Tectonophysics 730 (2018) 81–99

Contents lists available at ScienceDirect

Tectonophysics

journal homepage: www.elsevier.com/locate/tecto

Thermal structure of the Panama Basin by analysis of seismic attenuation

Carlos A. Vargas[a,*], José E. Pulido[a], Richard W. Hobbs[b]

[a] Universidad Nacional de Colombia, Department of Geosciences, Bogotá, Colombia
[b] Durham University, Durham, United Kingdom

ARTICLE INFO

Keywords:
Thermal structure
Panama Basin
Seismic attenuation
Curie point depth
Heat flow

ABSTRACT

Using recordings of earthquakes on Oceanic Bottom Seismographs and onshore stations on the coastal margins of Colombia, Panama, and Ecuador, we estimate attenuation parameters in the upper lithosphere of the Panama Basin. The tomographic images of the derived coda-Q values are correlated with estimates of Curie Point Depth and measured and theoretical heat flow. Our study reveals three tectonic domains where magmatic/hydrothermal activity or lateral variations of the lithologic composition in the upper lithosphere can account for the modeled thermal structure and the anelasticity. We find that the Costa Rica Ridge and the Panama Fracture Zone are significant tectonic features probably related to thermal anomalies detected in the study area. We interpret a large and deep intrinsic attenuation anomaly as related to the heat source at the Costa Rica Ridge and show how interactions with regional fault systems cause contrasting attenuation anomalies.

1. Introduction

Seismic attenuation is a measure of the energy dissipation of seismic waves as they spread inside the Earth. Observational and experimental data suggest that this phenomenon is controlled by the temperature, the mineral composition, and the presence of melts, fluids, volatiles, and cracks (Sato et al., 1989; Karato, 1993; Fehler and Sato, 2003; Artemieva et al., 2004). The attenuation parameter derived from the coda of S-waves, or the inverse of the seismic quality factor (Q^{-1}), depends on the frequency and the travel time, and consequently on the travel-path from the hypocenter of the earthquake to the seismic station (Singh and Herrmann, 1983; Jin and Aki, 1988), which makes it a suitable tool for investigating the sub-seismic structure lithosphere.

Attenuation is generated by two phenomena: (1) scattering (Q_{sc}^{-1}), which is a diffusion process of seismic energy due to interaction of the waves with heterogeneities in the lithosphere; and (2) intrinsic absorption (Q_{in}^{-1}), that represents the conversion of elastic energy into other forms of energy (e.g. heat or piezoelectricity). The combination of these parameters is responsible for the total observed attenuation. Hence, quantifying the contribution of Q_{sc}^{-1} and Q_{in}^{-1} has been a subject of considerable interest because offers information about internal structure and processes in the Earth interior (Vargas et al., 2004; Del Pezzo, 2008; Sato et al., 2012; Prudencio et al., 2013; Del Pezzo et al., 2016). Discrimination these two parameters can be estimated through multiple scattering models (Zeng, 1991; Hoshiba, 1991) or by using a hybrid approach, e.g. using the simple backscattering hypothesis and a multiple scattering model (Wennerberg, 1993).

A simple method for estimating the coda waves' attenuation under the simple backscattering hypothesis was proposed by Aki and Chouet (1975), who suggested that the parameter coda-Q (Q_c) is: (1) independent of recording site and event location; (2) independent of earthquake magnitude for events with $M < 6$; and (3) it has a close relationship with the local geology of the recording site. This method has been used widely to interpret the heterogeneity of the Earth (Fehler and Sato, 2003). However, there is not consensus regarding the meaning of Q_c^{-1} and its relationship with Q_{sc}^{-1} and Q_{in}^{-1} (Sato and Fehler, 2009). Notwithstanding, mapping these parameters offer valuable information about the lateral heterogeneities caused by tectonic domains and magmatic processes, as well as the thermal structure (Vargas and Mann, 2013; Prudencio et al., 2013; Del Pezzo et al., 2016).

Knowledge of the thermal structure of a region contributes to understanding its tectonic and magmatic behavior, as well as allowing inferences about its evolution and composition. The main approach for estimating the thermal structure is by using direct information from heat-flow measurements. However, these measurements are mainly limited to conductive heat-flow in sediments which can be perturbed by local fluid-flow. Fortunately, recent improvements in the estimation of the Curie Point Depth (CPD) based on analysis of magnetic anomaly datasets provides an alternative method for inferring the thermal structure of broad areas (Spector and Grant, 1970; Ravat, 2004; Ross et al., 2004; Vargas et al., 2015; Salazar et al., 2017). This regional approach allows the estimation of the depth at which magnetic minerals transit from ferromagnetic to paramagnetic states due to the effect of rising temperature. Many of these studies contrast heat-flow

* Corresponding author.
E-mail address: cavargasj@unal.edu.co (C.A. Vargas).

https://doi.org/10.1016/j.tecto.2018.02.017
Received 9 June 2017; Received in revised form 21 February 2018; Accepted 25 February 2018
Available online 08 March 2018

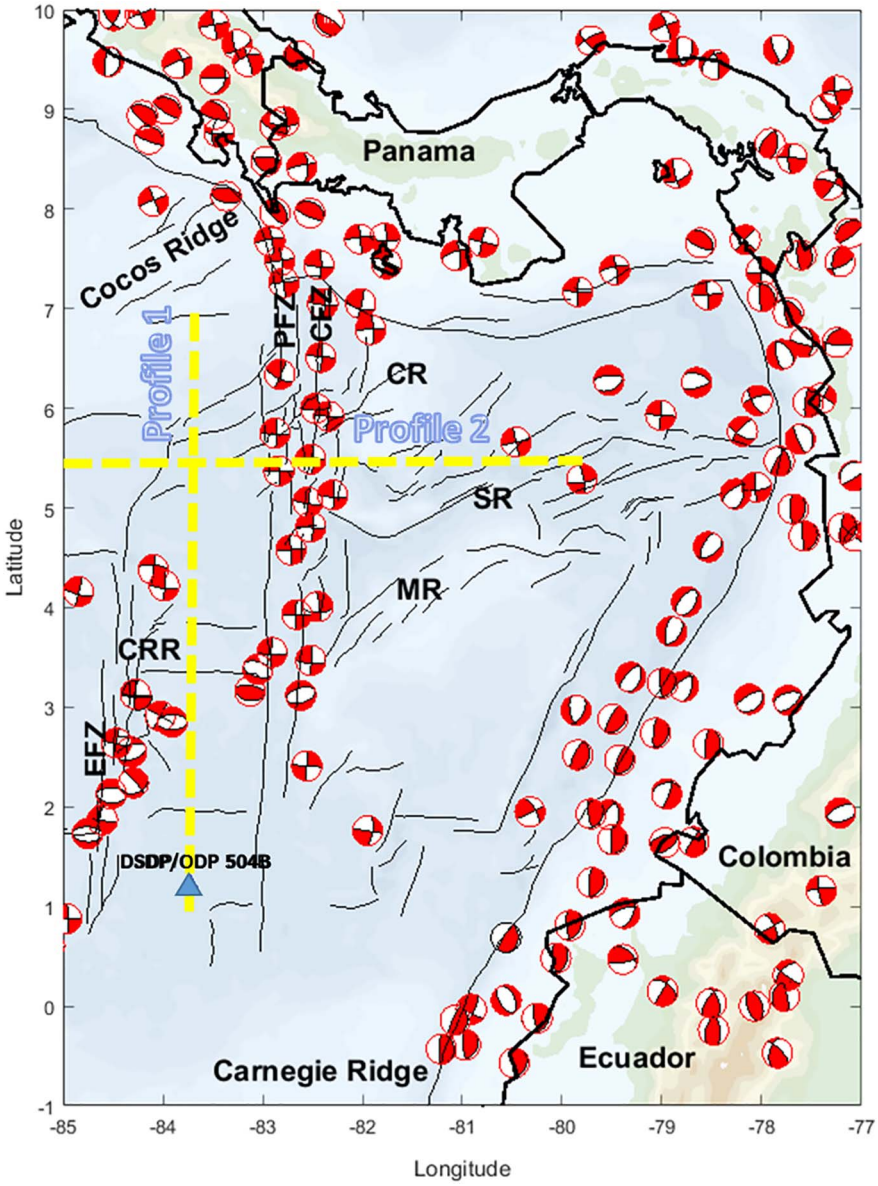

Fig. 1. Main tectonic features of the Panama Basin (thin-black lines). Shorelines are presented in bold-black lines. SR: Sandra Rift; MR: Malpelo Ridge; PFZ: Panama Fracture Zone; EFZ: Ecuador Fracture Zone; ER: Ecuador Ridge; CFZ: Coiba Fracture Zone; CR: Coiba Ridge; CRR: Costa Rica Ridge. Focal Mechanisms are extracted from the Global CMT Catalogue (Ekström et al., 2012). Blue triangle shows the location of the well DSDP/ODP 504B. Two dashed-yellow lines correspond to tomographic profiles discussed later. (For interpretation of the references to colour in this figure legend, the reader is referred to the web version of this article.)

observations and CPD estimations (Tanaka et al., 1999; Ruiz and Introcaso, 2004; Yang et al., 2017) for investigating the distortion of the thermal structure in the lithosphere.

In this study, we analyze the attenuation properties of the Panama Basin by discriminating Q_{sc}^{-1} and Q_{in}^{-1} based on Q_c^{-1} and Q_S^{-1} observations. This region offers an important opportunity to correlate the spatial distributions of these attenuation parameters with its thermal structure, which is associated to the formation and interaction of young lithospheric plates. The resulting attenuation structure is compared with Curie Point Depth (CPD) calculations using magnetic anomalies reported by Maus et al. (2007) and Dyment et al. (2015), and from direct observations of heat flow in the basin (Davis et al., 2004; Hasterok et al., 2011; Kolandaivelu et al., 2017).

2. Geotectonic setting

The Panama Basin is an area enclosed by the continental margins of Ecuador, Colombia and Panama to the East and North, and the Carnegie and Cocos ridges to the south and northwest (Fig. 1). It sits within the Galapagos gore, a region of oceanic crust formed at the Cocos-Nazca spreading center, east of the East Pacific Rise (Hardy, 1991). Our study focuses on the eastern part of the basin whose prominent features include the Panama Fracture Zone (PFZ), the Costa Rica Ridge (CRR), the Ecuador Fracture Zone (EFZ), and the Malpelo (MR), Coiba (CR) and Sandra ridges (SR). The formation of the basin was caused by the split of the oceanic Farallon plate into Cocos and Nazca plates at the beginning of the Miocene (Lonsdale, 2005) and interaction with the Galapagos hot-spot. Currently, the basin is moving eastward relative to South America with seismic activity primarily along the continental margins where focal mechanisms suggest extensional processes in proximal areas to the trench and compressional processes associated to the subduction of the Nazca Plate. The N-S orientated PFZ, EFZ and CFZ show focal mechanisms related to right-lateral movement, and the CRR and other ridges show a diversity of focal mechanisms. There is also seismic activity along other east-west structures related to the SR but this is less well constrained compared to that of the continental margins

and fracture zones.

The combination of sparse distribution of conductive heat flow measurements and the effects of regions dominated by advective heat loss limits the understanding of the thermal structure of the area by direct observation (Davis et al., 2004; Kolandaivelu et al., 2017). Spreading ridges, like the CRR, are known to be regions with active magmatic systems where the conductive heat flow is perturbed by hydrothermal processes. Also, the measurements are not evenly distributed over the area with a concentration around the site of the DSDP/ODP 504B borehole which was drilled in 6.9 Ma oceanic crust about 230 km south of the CRR.

3. Data and methods

New seismological dataset used in this study was collected during the cruise JC114 in 2015 as part of the OSCAR project (Hobbs and Peirce, 2015; Kolandaivelu et al., 2017). A multidisciplinary effort carried out in the Panama Basin that studies the coupling of heat- and mass-flow between the ocean and the lithosphere, together with its impact on the evolution of the oceanic crust and basin-scale circulation. For purposes of the seismic attenuation analysis, we use seismological records from eight Oceanic Bottom Seismographs (OBS) deployed to record the passive and active seismic activity during the OSCAR project. Together with the records from 17 permanent land stations administrated by the national seismological networks of Colombia, Panama, and Ecuador (Table Appendix A). A total of 352 events are located and analyzed with $M_D \leq 4.2$ during the time window January – March 2015 (Fig. 2a). Hypocentral solutions were estimated with the program Hypocenter (SEISAN ver. 10.5.0, Ottemöller et al., 2016). Events are selected with depths that range between 0 and 30 km, and RMS time residual of < 1.0 s, which reduces our dataset to 242 events.

3.1. Estimation of the attenuation parameters

To discriminate attenuation parameters, we use the Wennerberg's (1993) method, which is based on comparing the single-backscattering (Aki and Chouet, 1975) and the multiple-scattering (Zeng, 1991) attenuation models, under assumption that $Q_{\text{in}}{}^{-1}$ increases at rate of $e^{(-\omega t Q_{in}{}^{-1})}$. This method suggests that is possible to express $Q_{sc}{}^{-1}$ and $Q_{\text{in}}{}^{-1}$ based on observed values of $Q_S{}^{-1}$ and $Q_c{}^{-1}$ and using the relationships:

$$Q_S^{-1} = Q_{sc}^{-1} + Q_{\text{in}}^{-1} \tag{1}$$

$$Q_c^{-1} = Q_{\text{in}}^{-1} + [1 - 2\delta(\tau)]Q_{sc}^{-1} \tag{2}$$

where

$$[1 - 2\delta(\tau)] = -1/(4.44 + 0.738), \text{ and } \tau = \omega t Q_S^{-1}$$

and where ω is the angular frequency, and t is the lapse time. Combining Eqs. (1) and (2), we have:

$$Q_{sc}^{-1} = [Q_S^{-1} - Q_c^{-1}(\tau)]/2\delta(\tau) \tag{3}$$

$$Q_{\text{in}}^{-1} = [Q_c^{-1}(\tau) + (2\delta(\tau) - 1)Q_S^{-1}]/2\delta(\tau) \tag{4}$$

Eqs. (1) and (4) are used for finding $Q_S{}^{-1}$ as a positive root of a quadratic equation (Tselentis, 1998).

3.2. Estimation of the $Q_c{}^{-1}$

Following Aki and Chouet (1975) $Q_c{}^{-1}$ is estimated using the following equation:

$$P(\omega, t) = [2g(\pi)|S(\omega)|^2 \bullet e^{(-\omega t Q_c^{-1})}]/\beta t^2 \tag{5}$$

In this formulation, $P(\omega, t)$ is the time-dependent coda power spectrum, ω is the angular frequency, β represents the shear wave velocity, $|S(\omega)|$is the source spectrum and $g(\theta)$ signifies the directional scattering coefficient, defined as 4π times the fractional loss of energy by scattering per unit travel distance of primary waves and per unit solid angle at the radiation direction θ measured from the direction of primary wave propagation ($\theta = \pi$ for backward scattering). Geometrical spreading is proportional to r^{-1}, where r is the hypocentral distance, and applies only to body waves assuming a uniform medium. The source factor can be treated as a constant value for a single frequency, thus in Eq. (5) $Q_c{}^{-1}$ can be obtained as the slope of the least-squares fit of $ln[t^2P(\omega, t)]$ versus ωt, for $t > 2t_\beta$, where t_β is the S-wave travel time (Rautian and Khalturin, 1978; Vargas et al., 2004). The time-dependent coda power spectrum is normally calculated as the mean squared amplitudes of the coda $A_{obs}(f|r, t)$ from bandpass filtered seismograms.

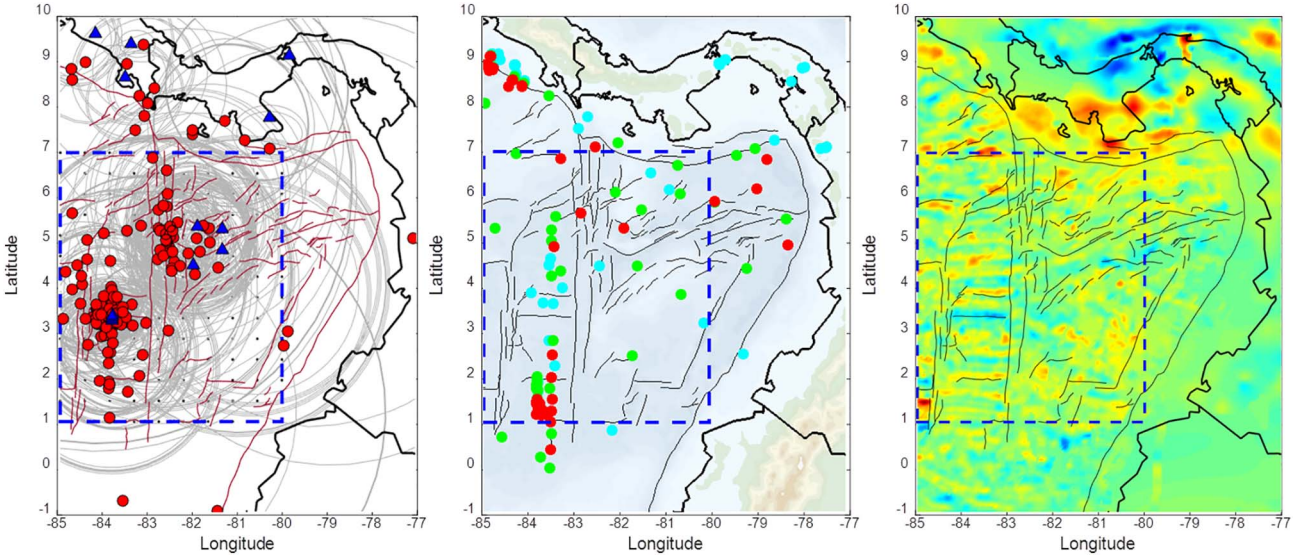

Fig. 2. Left: Red points represent the epicenter location of the seismic events used in the attenuation analysis. Grey ellipses are horizontal projections of ellipsoids related to the sampled volume during the simple backscattering process (Aki and Chouet, 1975), using as foci each event-station pair. Center: Location of conductive heat flow measurements (coloured dots) reported by International Heat Flow Commission (see Hasterok et al., 2011) and Kolandaivelu et al. (2017). Measurements were classified in three ranges: 0–100 mW/m2 (Cyan); 100–200 mW/m2 (Green); and > 200 mW/m2 (Red). Right: Dataset window of the WDMAM (Dyment et al., 2015) used for estimation of the Curie Point Depth in the study area. Blue-dashed polygon represents an area where attenuation and thermal structure are jointly analyzed. (For interpretation of the references to colour in this figure legend, the reader is referred to the web version of this article.)

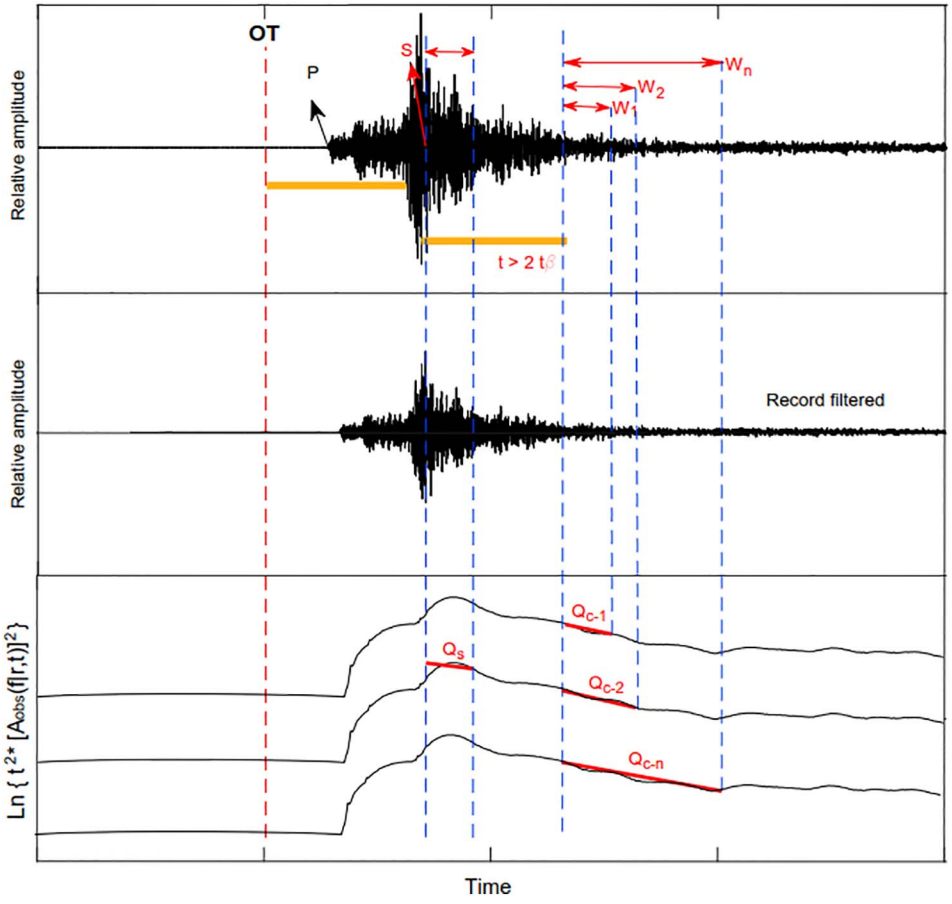

Fig. 3. Upper panel shows a seismogram of the vertical component recorded by an OBS station of the passive experiment around the Sandra Rift (Fig. 1). Origin time of the event (OT and red dashed line), as well as P and S phases are labeled. Attenuation analysis used signals arriving at $t > 1t_\beta$ for estimating Q_S^{-1}, Q_{sc}^{-1} and Q_{in}^{-1} values and at $t > 2t_\beta$ for estimating Q_c^{-1} values. First double-headed red arrow shows the S-coda wave. Intervals of signals W_1, W_2…, W_n, denote the different time lapse that were analyzed on each seismogram. Middle panel presents the seismogram filtered, which is used to estimate the energy envelope of the event (lower panel). Thus, Q_c^{-1} can be obtained as the slope of the least-squares fit of $ln\,[t^2|A_{obs}(\omega|r,t)|^2]$ versus ωt, for $t > 2t_\beta$, where t_β is the S-wave travel time (Rautian and Khalturin, 1978; Vargas et al., 2004). Blue dashed lines represent the time lapse windows used for estimating Q_S^{-1} and Q_c^{-1} values. (For interpretation of the references to colour in this figure legend, the reader is referred to the web version of this article.)

We used the program SEISAN (Ottemöller et al., 2016) for estimating the Q_c^{-1} values around center frequencies of 6.0, 9.0, 12.0, 15.0 and 20.0 Hz with the respective bandwidths of 1.5, 3.0, 3.0, 3.0 and 5.0 Hz, with signal to noise ratio ≥ 2, and S-wave velocity $\beta = 3.5\ km\ s^{-1}$. Only Q_c^{-1} values obtained from a least-squares fit with correlation coefficients > 0.7 were kept. Q_c^{-1} values were estimated for the lapse times (W) of 2.5, 5.0, 10.0, 15.0, 20.0 and 25.0 s, for each station and each frequency band (Fig. 3). In this work, we report only Q_c^{-1} values computed from the vertical component of seismograms as the horizontal components offer approximately the same range of estimated values for each frequency and W, which is consistent with the assumed isotropic model used, where the scattering process guarantees that the coda waves propagate with similar behavior in all directions, and therefore the attenuation parameters are comparable.

3.3. Estimation of Q_S^{-1}, Q_{sc}^{-1} and Q_{in}^{-1}

Q_S^{-1} values were estimated by using the spectral ratio method (Tsujura, 1966). The method uses the observed amplitude $A_{obs}(f)$ of body waves at the frequency f, which is related to the travel time t, the source to receiver distance r, the spectral amplitude at the source $A_0(f)$, and the response function of the site $R(f)$, with the following expression:

$$A_{obs}(f) \propto [A_0(f)R(f)e^{\pi f t Q_S^{-1}}]r^{-1} \quad (6)$$

Evaluating two frequencies f_1 and f_2, the natural logarithm of the ratio of the corresponding amplitudes can be expressed as:

$$ln\left[\frac{A_{obs}(f_1)}{A_{obs}(f_2)}\right] = ln\left[\frac{A_0(f_1)}{A_0(f_2)}\right] + ln\left[\frac{R(f_1)}{R(f_2)}\right] - \pi(f_1 - f_2)tQ_S^{-1} \quad (7)$$

If $A_0(f_1)/A_0(f_2)$ and $R(f_1)/R(f_2)$ are constant and independent of travel time, the function $ln[A_{obs}(f_1)/A_{obs}(f_2)]$ plotted versus t, will display the slope $-\pi(f_1 - f_2)/Q$ (Mukhopadhyay et al., 2008). These expressions assume that Q_S^{-1} is constant over the frequency band evaluated and that the source spectrum is comparable for all the earthquakes analyzed. The last assumption is valid provided the events analyzed lie within a small magnitude range, which is true for our case. For estimating the Q_S^{-1} values we set $f_1 = 4.5$ Hz and $f_2 = 6.0$, 9.0, 12.0, 15.0 and 20.0 Hz, respectively, and lapse time $W = 5.0$ s. As the case of Q_c^{-1}, values obtained from a least-squares fit with correlation coefficients > 0.7 were considered. Having estimated the values of Q_c^{-1} and Q_S^{-1}, we used Eqs. (3) and (4) for calculating the Q_{sc}^{-1} and Q_{in}^{-1} values.

3.4. Dependence of attenuation on frequency

Evaluating the frequency dependence of the seismic attenuation is a fundamental issue in observational seismology for the spatial-temporal characterization of the active and inactive tectonic areas worldwide. To evaluate dependence of attenuation on frequency, we fitted the Q_c^{-1}, Q_S^{-1}, Q_{sc}^{-1} and Q_{in}^{-1} values with the power law $Q^{-1}(f) = Q_0^{-1}(f/f_0)^{-\eta}$, where $f_0 = 1$ Hz, and the exponential term η determines the significance of the frequency dependence.

Table 1 shows the distribution of the attenuation values, at different frequencies and different lapse times. Table 2 presents the best-fit power equations that show the relationship of attenuation with the frequency.

3.5. Mapping the seismic attenuation (Q^{-1})

Malin (1978) expanded spatial concepts proposed by Aki and Chouet (1975), and suggested that the first-order scatterers responsible for the generation of coda waves at a given lapse time are located on the surface of an ellipsoid having earthquake and station locations as foci

Table 1
Variations of Q_c^{-1}, Q_s^{-1}, Q_{sc}^{-1} and Q_{in}^{-1} at different center frequencies and lapse time windows. Empty cells associated to some frequencies and lapse time windows correspond to no available information due to estimations do not guarantee confident values in agreement with the least-squares fit with correlation coefficients > 0.7 (see Section 3.2), which could be related with high levels of noise, mainly at the range of frequencies centered between 12 and 15 Hz.

Frequency (Hz)	Q_S^{-1}	Lapse time window 2.5 s			Lapse time window 5.0 s		
		Q_c^{-1}	Q_{sc}^{-1}	Q_{in}^{-1}	Q_c^{-1}	Q_{sc}^{-1}	Q_{in}^{-1}
	$\times 10^{-3}$						
6	24.4 ± 14.4	17.9 ± 12.2	21.9 ± 7.8	39.7 ± 15.7	7.9 ± 4.2	14.3 ± 12.9	10.7 ± 4.8
9	19.1 ± 14.9	20.8 ± 16.3	11.7 ± 5.8	32.5 ± 17.3	5.6 ± 2.9	15.4 ± 13.9	7.8 ± 3.5
12	20.4 ± 16.1	15.4 ± 10.5	11.3 ± 3.8	26.6 ± 13.2			
15	23.2 ± 19.6	13.7 ± 15.6	8.1 ± 4.2	21.8 ± 17.1			
20	22.2 ± 16.2	9.8 ± 11.6	8.6 ± 3.0	18.4 ± 13.3	3.3 ± 0.7	10.0 ± 10.7	4.6 ± 0.9

Frequency (Hz)	Lapse time window 10.0 s			Lapse time window 15.0 s		
	Q_c^{-1}	Q_{sc}^{-1}	Q_{in}^{-1}	Q_c^{-1}	Q_{sc}^{-1}	Q_{in}^{-1}
	$\times 10^{-3}$					
6	5.1 ± 2.2	17.0 ± 13.1	7.4 ± 2.6	3.4 ± 1.4	14.0 ± 7.3	5.2 ± 1.3
9	3.8 ± 1.3	9.9 ± 8.3	5.3 ± 1.6	2.7 ± 0.8	8.0 ± 5.6	3.9 ± 0.9
12						
15						
20	1.3 ± 0.1	29.0 ± 19.4	2.1 ± 0.3	1.3 ± 0.2	29.4 ± 18.9	2.1 ± 0.3

Frequency (Hz)	Lapse time window 20.0 s			Lapse time window 25.0 s		
	Q_c^{-1}	Q_{sc}^{-1}	Q_{in}^{-1}	Q_c^{-1}	Q_{sc}^{-1}	Q_{in}^{-1}
	$\times 10^{-3}$					
6	2.0 ± 0.4	15.8 ± 8.0	3.7 ± 0.4	1.3 ± 0.1	28.3 ± 29.0	2.8 ± 0.4
9	2.2 ± 0.7	6.8 ± 4.2	3.2 ± 0.7	1.1	7.1	1.9
12						
15						
20	1.2 ± 0.0	43.2 ± 2.4	2.0 ± 0.0			

(Pulli, 1984; Pujades et al., 1990). Other approaches considering the interpolation of mid-points between foci (Singh and Herrmann, 1983; Vargas et al., 2004); raytracing of paths through a given velocity model (e.g. Eberhart-Phillips and Michael, 1993; Thurber and Eberhart-Phillips, 1999; Wang et al., 2017); and using average values along the paths of the foci (Calvet et al., 2013). Mapping the multiple scattering processes of the coda wave is a challenge, due to its strong dependence with anelastic anomalies around the foci.

In this work, we have used the approach suggested by Vargas and Mann (2013) based on the hypothesis of single scattering, for inverting the 3D distribution of the Q_c^{-1} values. We also tested the approach presented by Prudencio et al. (2013) based on the hypothesis of multiple scattering for estimating the spatial distribution of the Q_{sc}^{-1} and Q_{in}^{-1} values. Finally, we evaluated the Calvet et al. (2013) approach, which minimized the problem in 2D by using a simple average of Q^{-1} values on cells distributed along the path of the foci.

3.5.1. Mapping Q_c^{-1}

The ellipsoidal volume sampled by coda waves at any time t, has a large semi-axis $a_1 = \beta t/2$, and the small semi-axis $a_2 = a_3 = (a_1^2 - r^2/4)^2$, where r is the source–receiver distance of the ellipsoid (Malin, 1978; Vargas and Mann, 2013). The average lapse time is related to an ellipsoidal shell, which is defined as $t_c = t_{start} + W/2$, being $t_{start} = 2t_\beta$, and W the coda-wave time window analyzed. Thus, knowing the values of t_c, W, and β, we can estimate the volumes of ellipsoidal shells where the seismic energy is scattered (Fig. 4). As we estimate Q_c^{-1} values for several values of W starting from t_{start}, we have redundancy in the volume sampled near to the ellipsoidal envelope that represents the

Table 2
Power law fitting of observations presented in Table 1 for several lapse time windows.

	Lapse time window 2.5 s	Lapse time window 5.0 s
$Q_S^{-1}(f) = (35.21 \pm 0.10) \times 10^{-3} * f^{-(0.33 \pm 0.01)}$	$Q_c^{-1}(f) = (76.70 \pm 4.35) \times 10^{-3} * f^{-(0.86 \pm 0.02)}$ $Q_{sc}^{-1}(f) = (27.43 \pm 0.68) \times 10^{-3} * f^{-(0.45 \pm 0.01)}$ $Q_{in}^{-1}(f) = (101.11 \pm 7.42) \times 10^{-3} * f^{-(0.86 \pm 0.03)}$	$Q_c^{-1}(f) = (29.62 \pm 0.60) \times 10^{-3} * f^{-(0.78 \pm 0.01)}$ $Q_{sc}^{-1}(f) = (46.50 \pm 0.48) \times 10^{-3} * f^{-(0.83 \pm 0.01)}$ $Q_{in}^{-1}(f) = (48.18 \pm 1.01) \times 10^{-3} * f^{-(0.79 \pm 0.01)}$

Lapse time window 10.0 s	Lapse time window 15.0 s	Lapse time window 20.0 s
$Q_c^{-1}(f) = (49.46 \pm 5.83) \times 10^{-3} * f^{-(1.24 \pm 0.05)}$ $Q_{sc}^{-1}(f) = (31.05 \pm 1.34) \times 10^{-3} * f^{-(0.54 \pm 0.02)}$ $Q_{in}^{-1}(f) = (61.24 \pm 7.84) \times 10^{-3} * f^{-(1.13 \pm 0.06)}$	$Q_c^{-1}(f) = (21.42 \pm 1.38) \times 10^{-3} * f^{-(1.03 \pm 0.03)}$ $Q_{sc}^{-1}(f) = (9.92 \pm 0.28) \times 10^{-3} * f^{-(0.03 \pm 0.01)}$ $Q_{in}^{-1}(f) = (27.62 \pm 2.76) \times 10^{-3} * f^{-(0.96 \pm 0.05)}$	$Q_c^{-1}(f) = (5.30 \pm 0.73) \times 10^{-3} * f^{-(0.52 \pm 0.06)}$ $Q_{sc}^{-1}(f) = (5.44 \pm 0.20) \times 10^{-3} * f^{-(0.34 \pm 0.01)}$ $Q_{in}^{-1}(f) = (5.30 \pm 0.73) \times 10^{-3} * f^{-(0.52 \pm 0.06)}$

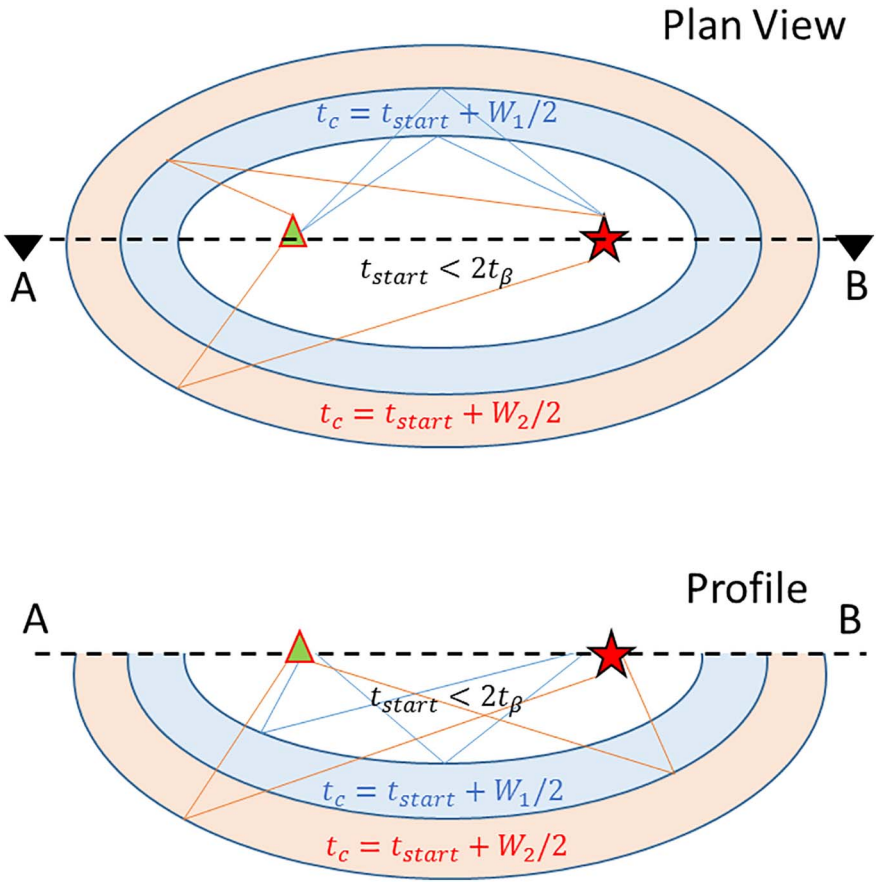

Fig. 4. Horizontal projection of the ellipsoidal volume sampled by coda waves at any time t, which has a large semi-axis $a_1 = \beta t/2$, and the small semi-axis $a_2 = a_3 = (a_1^2 - r^2/4)^2$, where r is the source (red star) – receiver (green triangle) distance of the ellipsoid (upper panel). The average lapse time is related to an ellipsoidal shell, which is defined as $t_c = t_{start} + W/2$, being $t_{start} = 2t_\beta$, and W the coda-wave time window analyzed. Lower panel represents a profile that suggest that expanding t_c or W, we can expect larger depths and volumes sampled. (For interpretation of the references to colour in this figure legend, the reader is referred to the web version of this article.)

instant t_c. As ${Q_c}^{-1}$ values have lapse time dependence (see Tables 1 and 2), then the spatial distribution of this parameter estimated for low t_c values correspond to small sampled volumes near to the foci with higher attenuation, and vice versa.

Based on assumptions stated above, we can achieve a generalized inversion for estimating the spatial distribution of ${Q_c}^{-1}$. This inversion requires a geographic grid around all foci considered. Each one of the ${Q_c}^{-1}$ values represents the attenuation average or apparent (${Q_{av}}^{-1}$) enclosed by the foci, whose values are related to the ellipsoidal shell given by

$$\frac{V_{TOTAL}}{Q_{av}} = \sum_j \frac{V_{Block-j}}{Q_j} \tag{8}$$

where $V_{Block-j}$ is the portion of volume (block) sampled by the ellipsoidal shell with the true attenuation parameter ${Q_j}^{-1}$ (or ${Q_{true}}^{-1}$). Assuming a constant β, we can determine the volume sampled by a ray that travels from the hypocenter and interacts with the ellipsoidal shell defined by the observation time of the coda where it is scattered to the receiver. So, the observed ${Q_{av}}^{-1}$ value can be represented as a sum:

$$Q_{av}^{-1} = Q_1^{-1}\frac{V_{Block-1}}{V_{TOTAL}} + \ldots + Q_{n1}^{-1}\frac{V_{Block-n}}{V_{TOTAL}} \tag{9}$$

where ratio $V_{Block-j}/V_{TOTAL}$ is the volume fraction related with the total scattered-wave travel path spent in the j^{th} block enclosed in the ellipsoidal shell. The process is repeated for all foci considered (k). This formulation can be expressed as a system of k-equations with n-unknowns, where $y = {Q_{av}}^{-1}$, $x_i = {Q_i}^{-1}$ and $a_i = V_{Block-i}/V_{TOTAL}$, or as compact matrix equation $\boldsymbol{AX} = \boldsymbol{Y}$, being $\boldsymbol{A}$ the $(k \times n)$ coefficient matrix, $\boldsymbol{X}$ the $(n \times 1)$ unknowns vector (total number of blocks), and $\boldsymbol{Y}$ the $(k \times 1)$ vector of observations. The system can be solved by an iteratively damped least-squares technique using the Levenberg-Marquardt method (Pujol, 2007). Hence, solution and resolution matrixes can be found using the equations:

$$X = [A^T A + \sigma^2 I]^{-1} A^T Y \tag{10}$$

$$R = [A^T A + \sigma^2 I]^{-1} A^T A \tag{11}$$

Spatial inversion of attenuation was performed using 529 observations of ${Q_c}^{-1}$ and an array of $10 \times 14 \times 8$ blocks located in coordinate ranges of Longitude between 80°W and 85°W, and Latitude between 1°S and 7°N, with block dimensions of ~55 km (longitude) × ~63 km (latitude) × ~4.2 km (thickness) to detect regional structures. The stopping criteria for performing the inversion was either a maximum of 2000 iterations or a relative difference of solutions between two consecutive iterations < 0.0000001. Qualification of the robustness of the tomography result was based on three approaches: (a) solving a chequer-board test; (b) mapping the diagonal elements of the resolution matrix (RDE) by using Eq. (11); and (c) hit count of ellipsoidal shells in each block. Details of these estimators and indicators quality of the reliable areas of the tomography are presented in Appendix A.

3.5.2. Mapping ${Q_{sc}}^{-1}$ and ${Q_{in}}^{-1}$

Prudencio et al. (2013) presented a back-projection method to estimate the spatial distribution of the scattering and intrinsic attenuation. The method uses a space weighting function derived from numerical simulation of the transport equation. They suggested that a simple Gaussian type weighting function may represent the seismic attenuation process under the multiple scattering assumption. According to these authors, the scatters that are responsible for generating the coda before the lapse time W, are all located inside an ellipsoid with the major axis given by $e_{max} = v \cdot W/2$ and $e_{min} = \left(v \cdot \left[\frac{W}{2}\right]^2 - r^2\right)^{0.5}/2$. They estimated empirically two standard deviations (σ_1 and σ_2) related to the energy distribution during the diffusion process and the ellipsoid axis, $\sigma_1 = e_{max}/9$ and $\sigma_1 = e_{min}/9$, that gave a Gaussian distribution for mapping the intrinsic and scattering attenuation:

$$P(x,y,z) = \frac{1}{2\pi\sigma_x\sigma_y\sigma_z} \times exp\left(-\left(\frac{(x-x_0)^2}{2\sigma_x^2} + \frac{(y-y_0)^2}{2\sigma_y^2} + \frac{(z-z_0)^2}{2\sigma_z^2}\right)\right) \quad (12)$$

Spatial and inversion parameters used in this case were similar to the previous section. However, after testing several attempts to mapping attenuation under the hypothesis of multiple scattering, we found that this approach highlights areas around the located the foci (see Appendix A). Hence, we choose the approach based on the simple scattering hypothesis presented in the previous section for mapping the seismic attenuation in the study area.

3.6. Estimation of the curie point depth

The heat flow dataset (Fig. 2b) comprises records reported by International Heat Flow Commission (see Hasterok et al., 2011). Estimations of the Curie Point Depth (CPD), the depth where the remnant or induced magnetization of minerals in the lithosphere disappears, is based on data from the World Digital Magnetic Anomaly Map-WDMAM version 2.0 (Dyment et al., 2015, Fig. 2c). This isotherm is assumed to be related to the Curie point of the magnetite, which lies between 575 and 585 °C (Hurt et al., 1995).

At least three methods have been suggested for calculating the CPD from radial average power spectrum (RAPS) of magnetic anomalies datasets. Detailed descriptions of the Spectral Peak Method – SPM (Spector and Grant, 1970), the Centroid Method – CM (Okubo et al., 1985), and the Forward Modeling Method – FMM (Ravat, 2004; Ross et al., 2004), are presented in Salazar et al. (2017). Although we performed CPD estimations with all three methods, here we show results using the FMM. Then, we contrast the spatial distribution of CPD with the attenuation model and heat flow observations.

The CPD is estimated on the idea that average magnetization tends to zero below this isotherm. Based on this hypothesis, we assume the presence of a magnetic layer that spreads infinitely in all horizontal directions. The depth to the bottom of this layer is small compared with the horizontal scale of the magnetic source, and its magnetization field $M(x,y)$ can be expected as a random function of x and y. The power spectrum density of the magnetic anomalies can be expressed as (Blakely, 1996):

$$\Phi_{AT}(k_x,k_y) = \Phi_M(k_x,k_y) \bullet F(k_x,k_y) \quad (13)$$

$$F(k_x,k_y) = 4\pi^2C^2\,|\theta_m|^2\,|\theta_f|^2 e^{-2|k|Z_T} \bullet (1 - e^{-|k|(Z_c-Z_T)})^2 \quad (14)$$

where Φ_M is the power spectral density of the magnetization, k_x and k_y correspond to wave numbers along the coordinates x and y, respectively, C is a proportionality constant, θ_m and θ_f are factors of the direction of magnetization and the direction of the geomagnetic field, respectively. Eq. (14) is simplified by observing that all terms are radially symmetrical. If $M(x,y)$ is completely random and uncorrelated, $\Phi_M(k_x,k_y)$ is a constant. Therefore, the radial average of Φ_{AT} can be expressed as:

$$\Phi_{AT}(|k|) = Ae^{-2|k|Z_T} \bullet (1 - e^{-|k|(Z_c-Z_T)})^2 \quad (15)$$

where A is a constant, Z_c is the CPD, and Z_T is the depth to the top of the magnetic source. The numerical approximation for estimating the CPD using the forward modeling method uses a nonlinear least-squares fit of the right side of Eq. (16) with the square root of the RAPS of magnetic anomalies (Ross et al., 2004).

$$\Phi_{AT}(|k|^{0.5}) = C[e^{-|k|(Z_T)} - e^{-|k|(Z_c)}] \quad (16)$$

where C is an independent constant, Z_c and Z_T are changed iteratively to find the minimum error between the observed data and theoretical estimations. For these estimations, we used the database compiled in the WDMAM (Maus et al., 2007; Dyment et al., 2015). For the inversion, we selected a rectangular window of this database that ensured the dimension criterion of six times the depth of the target (Okubo et al., 1985). Given the database has a resolution of approximately 5.6 km, our analysis window for each CPD estimate is 336 km × 336 km. The window steps 5.6 km in both the x and y directions until the entire area is covered. Uncertainties of the calculations are estimated according to Okubo and Matsunaga (1994):

$$\varepsilon = \frac{\sigma}{k_2 - k_1} \quad (17)$$

where σ represents the standard deviation of the differences between the natural logarithm of the power spectrum density and data fitted by the least squares method. k_1 and k_1 express the boundary values of the wavelengths which are used in the Z_c estimation.

4. Results and analysis

4.1. Attenuation parameters

Following the procedures outlined in Sections 3.2 and 3.3, we found that the calculated values of ${Q_c}^{-1}$, ${Q_S}^{-1}$, ${Q_{sc}}^{-1}$ and ${Q_{in}}^{-1}$ decrease with the increase of the frequency (Table 1). The results show in general terms, that for small lapse time windows, the attenuation at all frequencies is higher than for large lapse time windows, and that ${Q_{sc}}^{-1}$ estimation is not robust. It is important to note that while the site response and source properties may not have a large affect the measured ${Q_c}^{-1}$, they can promote significant impact on the ${Q_S}^{-1}$ values measured from direct S-waves, and thus yield less reliable ${Q_{sc}}^{-1}$ and ${Q_{in}}^{-1}$ values.

We compare ${Q_c}^{-1}$ with the other attenuation parameters (Fig. 5). ${Q_c}^{-1}$ values are lower than ${Q_S}^{-1}$, ${Q_{sc}}^{-1}$ and ${Q_{in}}^{-1}$ for almost all frequencies for lapse time windows W > 10s. In addition, for low frequencies we note that ${Q_{in}}^{-1} > {Q_{sc}}^{-1}$. We test this observation (Table 2). For frequency f_0 = 1Hz, almost all the lapse time windows show a prevalence of intrinsic attenuation over that caused by scattering processes. ${Q_0}^{-1}$ and η, the frequency exponent, show the same trend for ${Q_c}^{-1}$ and ${Q_{in}}^{-1}$ in contrast with the ${Q_{sc}}^{-1}$ trend.

Attenuation tomography hypothesis suggests that larger sampled volumes (deeper and broader zones) are associated with larger lapse time windows (Vargas and Mann, 2013), from which we infer that the predominant intrinsic effects are located near to the seismic sources and that effects become weaker with distance from the source. This outcome is detected in the study area by the ${Q_{in}}^{-1}$ and ${Q_c}^{-1}$ values. High ${Q_{in}}^{-1}$ values are frequently related to zones with the presence of magmatic and/or hydrothermal systems, where composition, density and temperature have strong relationship on seismic attenuation (Lin et al., 2015).

Parameter $\eta \sim 1.0$ is often associated with tectonically active zones (Aki, 1980; Roecker et al., 1982; Akinci et al., 1994; Mukhopadhyay et al., 2008; Singh et al., 2014). In the study area, we found low values of η in the scattering attenuation (η_{sc}), but also ${Q_{in}}^{-1} > {Q_{sc}}^{-1}$ for low and intermediate values of lapse time windows (W = 2.5, 10 and 15 s). These observations suggest small contributions of the scattering in the total attenuation estimation, and that scattering behavior is probably located in small volumes near to the foci. In addition, as η_c and η_{in} are similar and nearer to 1.0 than η_{sc}, we infer a consistent attenuation behavior of tectonically active zones associated to magmatic and/or hydrothermal processes. It is probably that the low values of η_{sc} are related to shallow scattering processes located in more brittle layers of the study area. In fact, abrupt topography and strong faulting are frequently associated to this parameter (O'Brien and Bean, 2009), which is possible here.

4.2. Spatial distribution of attenuation and mapping the curie depth point

After synthetic tests for evaluating the resolution of the tomographic methods and dataset used (see Appendix A), we present four depth tomographic sections at 3, 13, 23 and 33 km measured from the sea-surface, with cell resolution of 0.5° × 0.5° located between 85°W - 80°W and 1°N–7°N, and vertical grid resolution of 4.1 km. The associated resolution tests show that the NW and SE areas have low reliability, although these zones appear to be significant anomalies. The poorly constrained resolution allows the inference that these areas are probably an artifact of the inversion (see Appendix A). Elsewhere within the

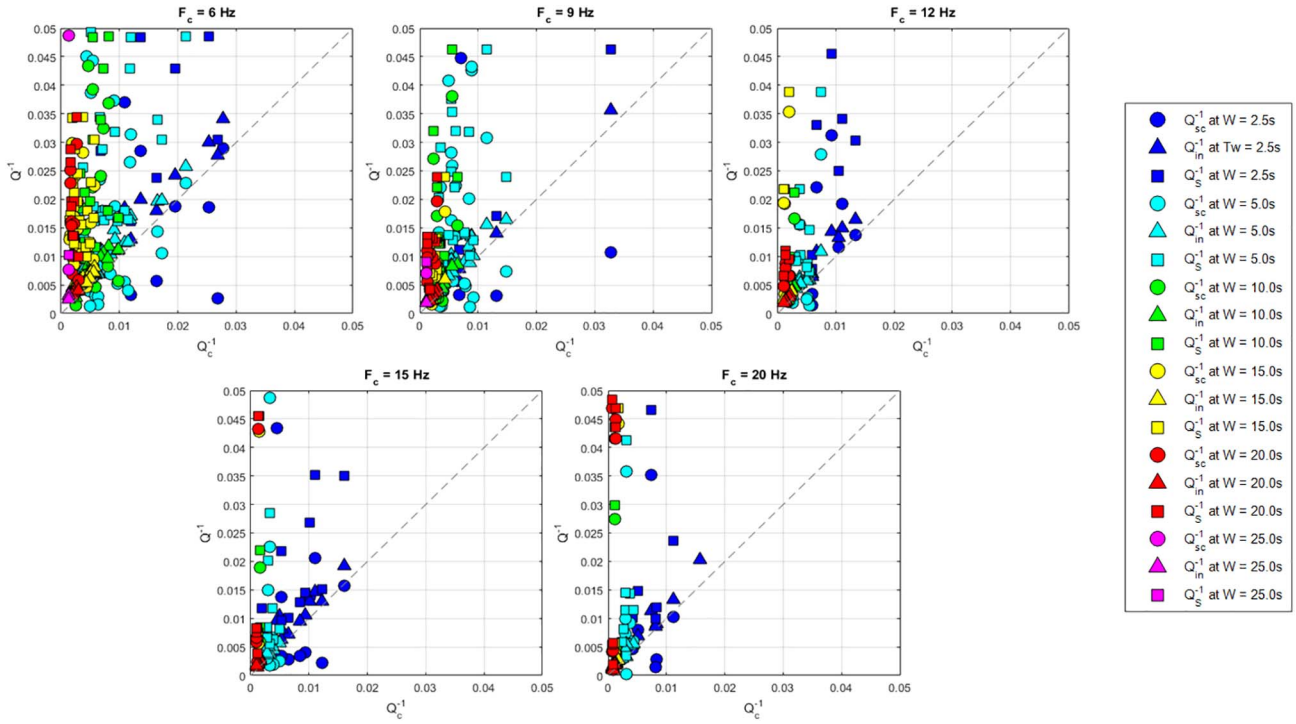

Fig. 5. Comparison of Q^{-1} at different lapse-times and frequencies. Note that for small lapse time windows, the attenuation at all frequencies is higher than for large lapse time windows.

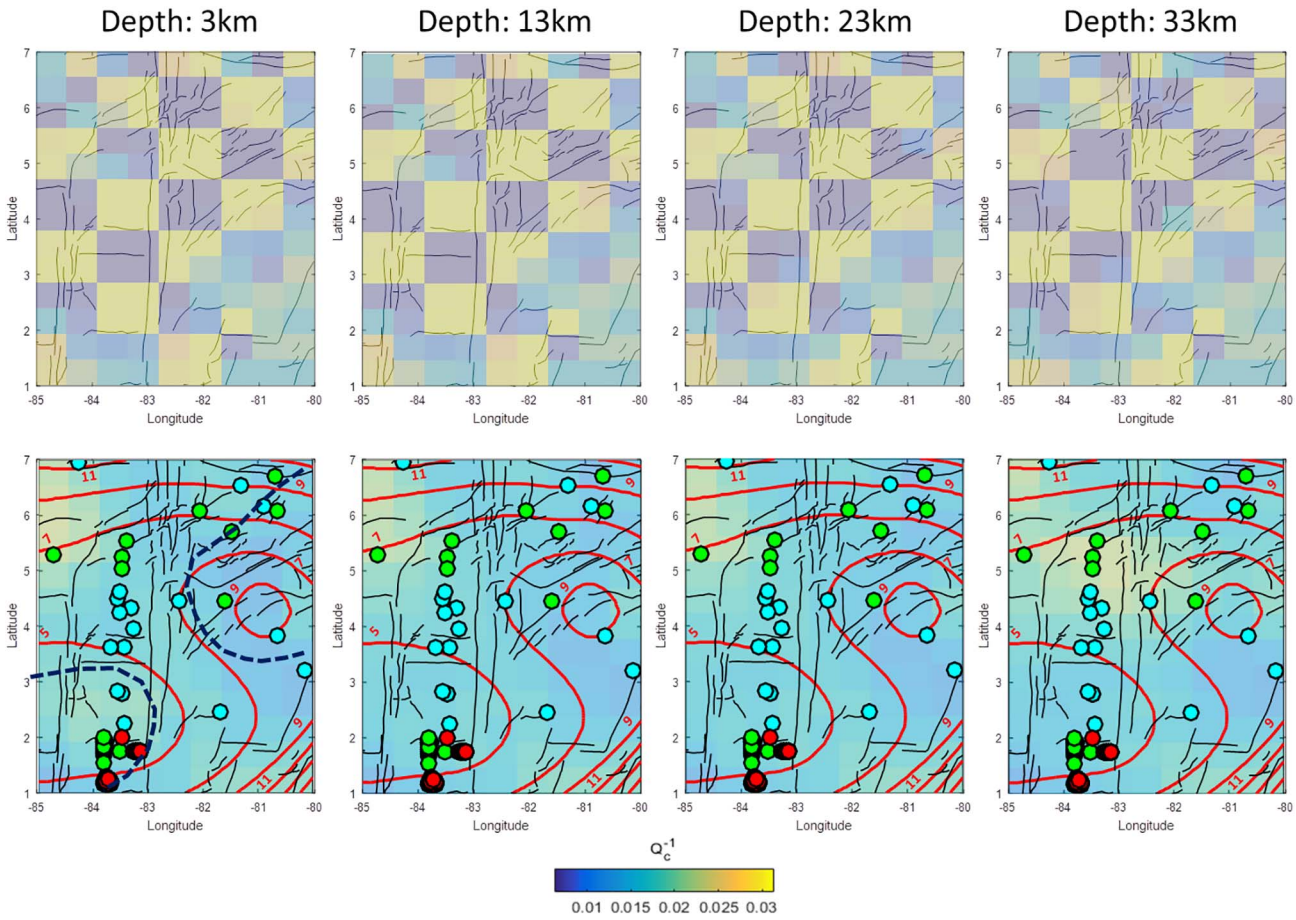

Fig. 6. Upper panel: four depth slices showing the results of chequerboard testing of the tomography cube at 3, 13, 23 and 33 km depth measured from the sea-surface using the methods described in Appendix B. The slices show that the volume is generally well constrained except for the SE and NW corners. Lower panel: spatial distribution of Q_c^{-1} anomalies at 6 Hz for the same depth slices overlaid with CPD contours (red). Four significant higher attenuation anomalies are visible. Dashed black lines in the shallowest section suggest the boundary of three possible thermal provinces. (For interpretation of the references to colour in this figure legend, the reader is referred to the web version of this article.)

body of the inversion cube, where there is reasonable constraint, there are four anomalies of note (Fig. 6). One located at south of the CRR, which extends from surface to the 13 km depth section. The second one is located at north of the CRR, which is observed only on the deepest sections. The third spreads between the north of the PFZ, the CFZ and CR which disappears at 13 km depth. The last one is in the central-eastern zone, south of the SR, which is consistent on all depth sections. Overlaying the Q_c^{-1} sections, are the estimated CPD contours that indicates the likely depth of this isotherm from the sea-surface in the study area so we can compare attenuation with CPD anomalies. Note the CPD is heavily smoothed by the inversion so it only provides the long wavelength trend and does not respond to specific features like the CRR. An uncertainty map of this isotherm is presented in Appendix B.

Fig. 6 shows that the estimated depth of the CPD shallows toward the SW, where structures like the EFZ and CRR are enclosed by the 5-km contour. South of the MR and SR there is an area where this isotherm is deepened. Comparing the depth to CPD isotherm and attenuation distribution, we identify three domains: 1) in SW, including areas of the CRR, EFZ and southern end of the PFZ, which present a shallower CPD and higher seismic attenuation; 2) the central zone of the study area which shows low attenuation and intermediate values of CPD along a NW-SE trend; and 3) the NE area where the CDP isotherm becomes deeper and the attenuation has slightly higher values.

5. Discussion

Experimental and observational contributions offer a broad vision of the relationship between the anelastic properties and the thermal structure in the Earth (Jackson et al., 1992; Karato, 1993). However, these associations are not well understood, as there are yet unknown parameters that limit the validity of proposed models (see, e.g. Artemieva et al., 2004). Fig. 5 is a good example of this scenario where beyond a general interpretation of the large domains, limitations of the dataset and model discrepancies of the methods and theory inhibit a more precise identification of underlying processes.

Nevertheless, our results allow to identifying some potentially interesting correlations between the analyzed parameters. Fig. 7 shows relationships between average values of conductive heat flow, for the locations where measurements are available, with the CPD and the Q_c^{-1} values estimated in each cell of the shallowest slice of the attenuation tomography (Fig. 6). With attention to the restrictions and the number of points evaluated that is limited by the number of cells with conductive heat-flow observations, we unsuccessfully tried to find spatial patterns in the conductive heat-flow measurements. Then, based on the uncertainty in the CPD values and limitations of the conductive heat-flow dataset given the likely effects of advective heat loss, we found that the observations show some weak trends between these parameters. For instance, we evaluated the relationship between CPD and heat-flow using the model (Tanaka et al., 1999; Ruiz and Introcaso, 2004; Maule et al., 2005):

$$HF = \lambda\frac{T_b - T_t}{Z_b - Z_t} + H_o hr^2\frac{e^{-Z_b/hr} - e^{-Z_t/hr}}{Z_b} + H_o hre^{Z_t/hr} \quad (18)$$

where λ is the coefficient of thermal conductivity, T_t and T_b are the top and bottom temperatures of the magnetic layer located at Z_t and Z_b depths respectively; H_o represents the heat production rate at the surface, and *hr* correspond to the characteristic drop off of H_o. We assumed that $T_b - T_t = 580\ K$, $Z_t = 0\ km$, $H_o = 3.0 \times 10^{-6}\mathrm{W/m^3}$, and $hr = 10\ km$ (Yang et al., 2017). The statistical fit of observations shows a correlation coefficient $|R^2| = 0.5536$, with $\lambda = 1.186$ and confidence boundaries of 95% (λ[0.974 1.389]). On the other hand, an empirical approach of the form $Q_c^{-1} = K_1 \cdot e^{K_2 \cdot HF} - K_3$ was used for correlating Q_c^{-1} and heat flow (see, e.g. Artemieva et al., 2004, Formula 3.10 for correlating Q^{-1} and temperature, where were expressed $K_1 = 0$, $K_2 = 0.00267$, and $K_3 = 6.765$). Our best fit shows a correlation coefficient $|R^2| = 0.8725$, with $K_1 = 0.4444$, $K_2 = 0.005696$, $K_3 = 3.9$, and confidence boundaries of 95% (K_2[0.006890 0.004502]). Finally, Q_c^{-1} and CPD fit to a model of the form $Q_c^{-1} = K_1 + K_2 \cdot e^{-K_3 \cdot CPD}$, where $K_1 = 0.0001$, $K_2 = 0.06$, $K_3 = 0.1687$, and confidence boundaries of 95% (K_3[0.1467 0.1906]). The correlation coefficient for this relationship is $|R^2| = 0.8340$. Differences amongst$|R^2|$ may be explained if we consider that Eq. 18 is supported by a widely-used specific model (see, e.g. Tanaka et al., 1999; Ruiz and Introcaso, 2004; Maule et al., 2005), but this model does not suit our dataset, probably due to other variables within the problem. Instead, for the case of Q_c^{-1} vs HF, and Q_c^{-1} vs CPD we used empirical approaches that have not been used previously in literature but that fit our observations much better. At present, without testing on other datasets, it is not yet possible to assign a physical meaning to the constants incorporated in these empirical formulas (K_n). Regardless, we should note that due to the dispersion of the dataset, there is a wide variety of models that may also match the observations. We also note that the Euclidean distance of RMS values between Q_c^{-1} and Q_{sc}^{-1} for all frequencies is approx. 11.6 times lower than those corresponding to Q_c^{-1} and Q_{in}^{-1}, meaning that for this study zone the processes that govern the intrinsic attenuation are probably related with the thermal structure. Hence, the scatter of points (Fig. 5b–d) may reflect contributions of the scattering process in thermally active areas, e.g. structures like CRR, EFZ, CFZ and PFZ. These are zones where there are hydrothermal processes that perturb the measured conductive heat flow. We speculate that in the east of the study area, the closeness to the continental margins may cause more faulting and consequently inducing an additional scattering effect on the seismic waves. We expect higher values of the CPD to be associated with older crustal ages and lower heat flow, but this pattern is not so clear. Another possible explanation is related to the contrasting lateral variations of age and composition in the upper crust of this region, e.g. CR and MR.

Fig. 8 presents two profiles of Q_c^{-1} values showing the CPD isotherm and heat flow measurements. Profile N-S, runs approximately through the center of the CRR segment and the DSDP/ODP 504B well. On this profile, the CPD is < 3 km depth from the sea-bed and becomes slightly deeper to the north. The theoretical heat flow trend derived from the half-space cooling model (Hasterok et al., 2011; Turcotte and Schubert, 2014) is shown for comparison with the observed conductive heat flow dataset. Near to the DSDP/ODP 504B well, the measured heat flow is consistent with that predicted by the cooling model as it is dominated by conductive heat loss. For the rest of the profile, north of DSDP/ODP 504B, the measured heat flow is significantly lower than that predicted by the cooling model. Here the heat loss is dominated by advection associated with hydrothermal processes in young ocean crust. The change from advected dominated heat flow to conductive heat flow coincides with a change from higher to lower attenuation. This may indicate a change in thermal properties or a possible change in seismic signal loss by scattering. It is also of note that the high attenuation region at depth could be interpreted as caused by the melting zone under the CRR, but its center is displaced about 100 km north of the current spreading axis.

The prominent attenuation anomaly located in the west sector of the profile positioned at latitude ~5.5°N (Fig. 8b) is not considered for interpretation due to the lower reliability of the inversion in this zone, but we focus on the anomaly under the MR, which is an older structure with respect to the surrounding crust (~17 Ma, Lonsdale, 2005). The increase in the attenuation and a CPD isotherm that becomes shallower in this area could be related to thermal processes, as is suggested by the high heat flow observation. We suggest that this attenuation anomaly corresponds to a combination of scattering processes caused by larger faulting and lateral heterogeneities, combined with a deep interaction with magmatic bodies or possibly hydrothermal processes. It is difficult to be sure about the origin of the weak deeper attenuation anomaly around ~30 km depth observed at east end of this profile. There is no direct evidence of magmatic processes, lateral variations of the lithospheric system, nor faulting, associated to the bending of the plate once

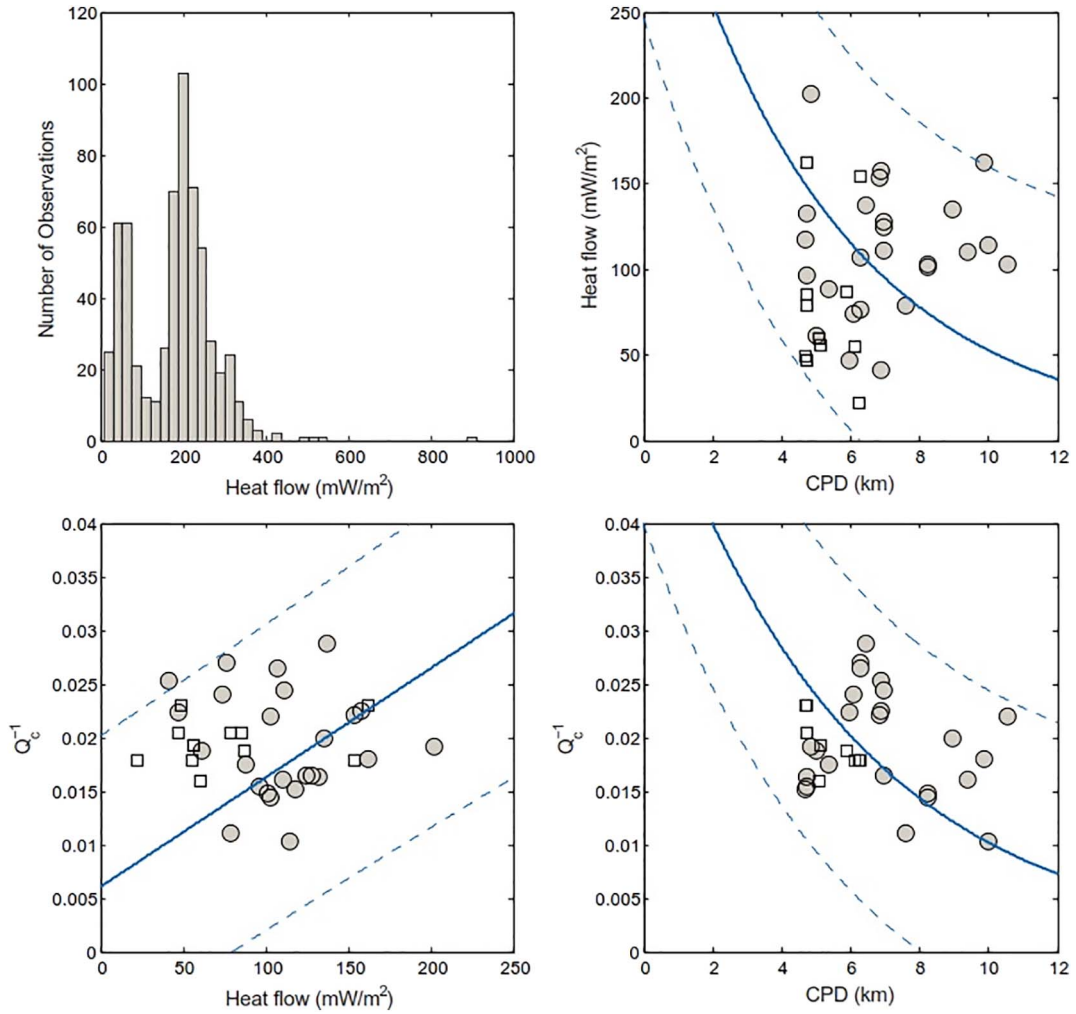

Fig. 7. Comparison of thermal parameters with Q_c^{-1} values at 6 Hz. Estimations of the CPD and measurements of conductive heat flow (grey circles) correspond to mean values on each cell of the shallowest section of the tomography. The black squares represent individual measurements over young ocean crust < 5 Ma that are significantly affected by advected heat loss. Continued blue lines represent the best fit models with 95% of confidence boundaries (dashed lines), according to the trends suggested in the main text. a) Histogram of heat flow measurements reported in the Panama Basin. b) Comparison between CPD and HF. c) Comparison between *HF* and Q_c^{-1}. d) Comparison between CPD and Q_c^{-1} values. (For interpretation of the references to colour in this figure legend, the reader is referred to the web version of this article.)

it converges to the continental margin, to explain this anomaly.

Major fault system zones are scenarios of different thermal conditions (see, e.g. Sutherland et al., 2017) where high attenuation is related to the presence of magmatic/hydrothermal activity or lateral variations of lithologic composition in the upper lithosphere. Where this contrast juxtaposes lithosphere with significant variation in lithology and/or age, it may be possible to characterize this difference by mapping the intrinsic or scattering attenuation of the seismic waves. A conceptual model for our attenuation tomography cube, as well as the CPD isotherm, superficial heat flow observations and regional faults is presented in Fig. 9. This model reinforces the existence of a deep source of attenuation beneath the CRR. Also, that the PFZ acts as a significant boundary between attenuation anomalies that can be seen on the upper surface of the tomography cube and at depth. This model suggests that a shallower trend in the CPD correlates with areas of higher attenuation, probably associated with thermal processes. The major faults play an important role in partition of the intrinsic attenuation, but their contribution on the scattering of the seismic energy is not dominant. Whereas regions of pervasive faulting and rough seabed topography between the CRR and DSDP/ODP 504B borehole caused by ocean crust formation processes may influence the measured attenuation anomaly. Discrimination of the causes of attenuation in the upper lithosphere offers an interesting perspective for the assessment of the thermal structure under different geological environments. We have tried to estimate values of temperature based on formulations suggested by Sato et al. (1989), Karato (1993), and Artemieva et al. (2004), however the large range of uncertainties, prevents us from producing a robust result for this endeavour.

6. Conclusions

Using the estimates of coda-Q, Q_c^{-1}, we estimate the contributions of intrinsic and scattering attenuation processes in the upper lithosphere of the Panama Basin. The derived tomographic images were compared with CPD estimates and heat flow measurements to evaluate the thermal structure of this region. We detect three tectonic domains where magmatic/hydrothermal activity or lateral variations of the lithologic composition in the upper lithosphere, are responsible of the current thermal structure and the anelastic behavior of the seismic propagation.

The ocean ridges and fracture zones constitute tectonic features of the study area where thermal processes of conduction and advection coexist. Under the Costa Rica Ridge, we have detected a large and deep intrinsic attenuation anomaly probably related to the heat source. We also show how regional fault systems may be detected by contrasting attenuation anomalies where they juxtapose crust of different lithology or age. Finally, we suggest that intrinsic attenuation, CPD and conductive heat flow may be correlated.

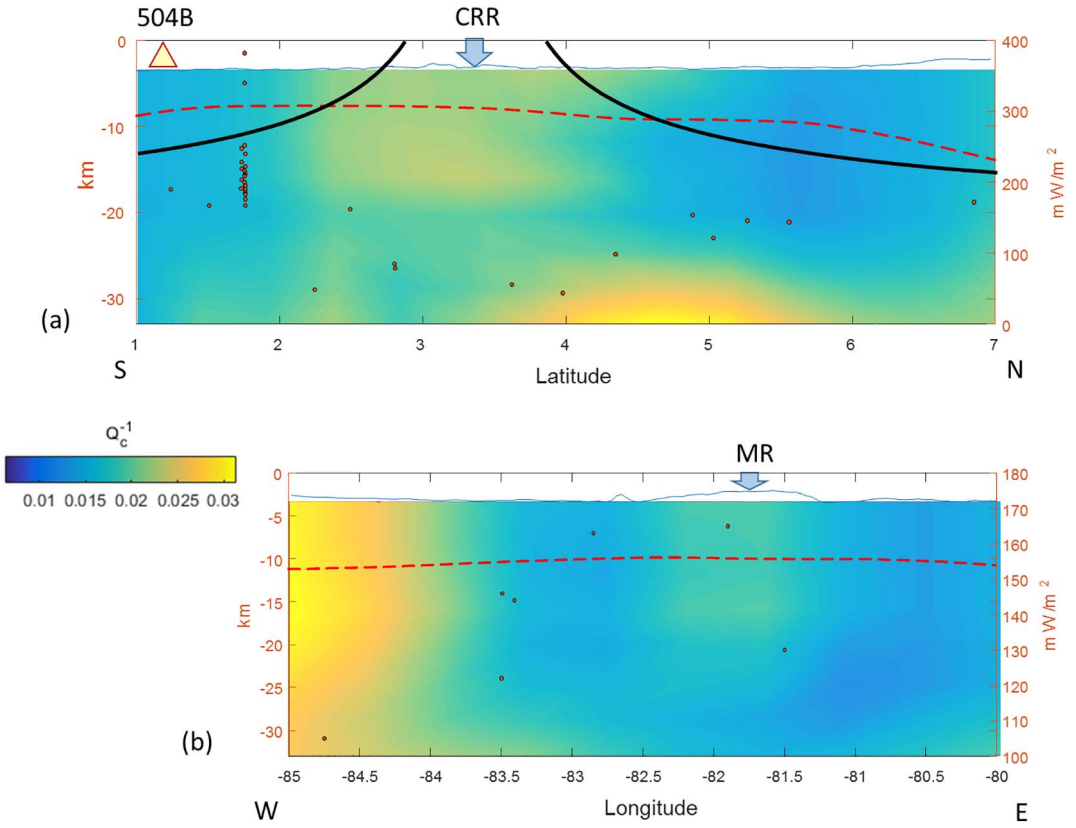

Fig. 8. Attenuation profiles along orientations (a) S-N between latitude 1–7 N, and (b) W-E between longitude 85-80 W (see location in Fig. 1). Profiles have double scale: Depth (km) in the left-side, and Heat Flow (mW/m^2) on the right-side. The profiles also show the CPD isotherm (red-dashed line), bathymetric profile (thin black line), the heat flow observations (brown circles) and, for profile (a), the theoretical heat flow response derived of the cooling half-space model (Hasterok et al., 2011; Turcotte and Schubert, 2014) (thick black line). Blue arrows show the location of the Malpelo Ridge (MR) and the Costa Rica Ridge (CRR) and the yellow triangle on the profile (a) represents the location of the ODP 504B well. Heat flow observations were taken from the Global Heat Flow Database of the International Heat Flow Commission, version 2010, http://www.heatflow.und.edu. (For interpretation of the references to colour in this figure legend, the reader is referred to the web version of this article.)

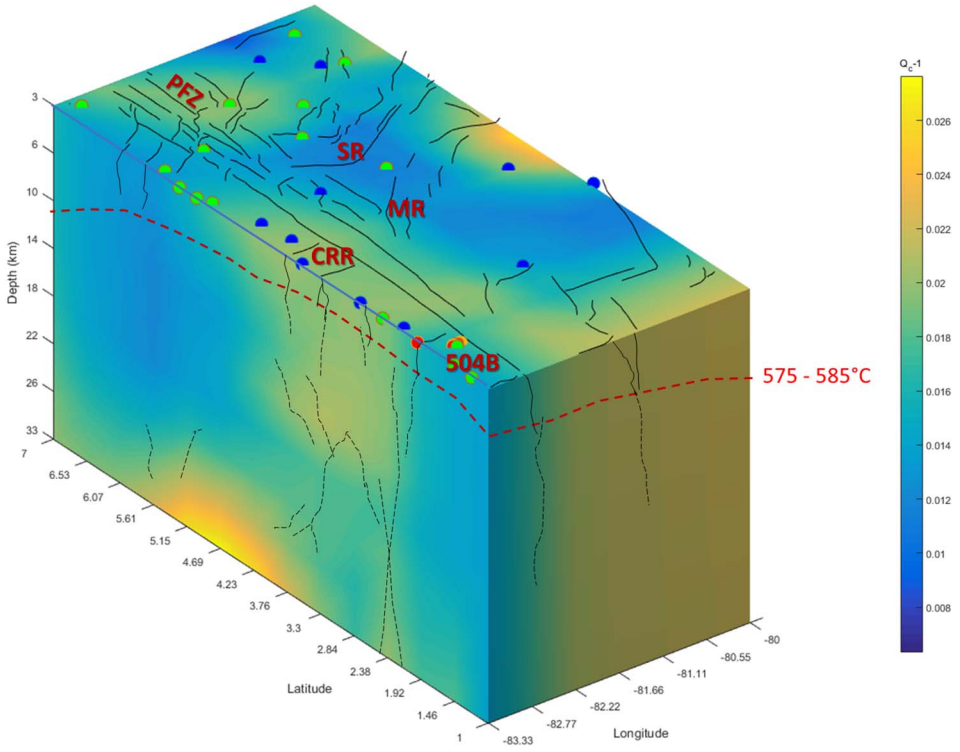

Fig. 9. 3D attenuation block showing the regional location of the CPD isotherm (575–585 °C) (red dashed line) and its relationship with Q_c^{-1} anomalies and fault systems. Significant tectonic features are marked on the top face of the cube where they can be confidently mapped from bathymetry. Speculative extension of these feature to depth are indicated by dotted lines. Of these, the boundary in the attenuation anomalies with the PFZ is of particular note. (For interpretation of the references to colour in this figure legend, the reader is referred to the web version of this article.)

Acknowledgements

CAV and JEP thank Universidad Nacional de Colombia, Department of Geosciences for helping support this research. RWH and CAV are gratefully to the Durham University and the NERC for supporting the research project OSCAR, grant NE/I027010/1 (Hobbs and Peirce, 2015). The authors thank the officers, crew, technicians and science party on board the RRS James Cook during cruise JC114 especially the OBIC staff for making the data collection possible. CAV thanks COLCIENCIAS for partial funding through Grant #FP44842-006-2016 (Análisis 4D de Vp, Vs y la relación Vp/Vs en la Esquina NW de Suramérica) and the Durham University Santander program, for a travel grant to support a sabbatical visit to Durham.

We thank Prof. Christine Pierce, Dr. Dean Wilson, Dr. Alexander Gonzalez-Najazawa and Emma Gregory of the Durham University for offering help during this research.

Earthquake data are available from the national seismological networks of Colombia, Panama, and Ecuador. The OSCAR OBS data can be obtained through the British Oceanography Data Centre (www.bodc.ac.uk).

Appendix A. Uncertainties of the 3D seismic attenuation tomography and the Curie Point Depth estimation

A. *Chequerboard test of attenuation inversion parameters*

Using two dissimilar Q^{-1} values (1/12 and 1/900, derived from the higher and lower values observed in the dataset) we have performed tests to evaluate the resolution of the spatial inversion under the single backscattering hypothesis using a 3D chequerboard. As the dataset is dominated by foci with frequencies centered at 6 Hz (529 observations), compared to other frequencies (352 at 9 Hz, 205 at 12 Hz, 184 at 15 Hz, and 139 at 20 Hz), the spatial estimations are presented in this frequency. Fig. A1 shows the results of inverting our dataset to reconstruct the chequerboard at four depth slices using the approach suggested by Vargas and Mann (2013). We see that spatial distribution of Q_c^{-1} is reliable for almost all the study area, with exception of areas located at SE an NW. Depth slices deeper than 23 km have less reliable results. Fig. A2 shows maps of the Resolution Diagonal Elements (RDE) derived for the inversion, as well as the number of times that the ellipsoidal shells cross each cell (N), which substantiates the solution shown in the chequerboard test. We repeated the calculations by using the approach presented by Prudencio et al. (2013). Fig. A3 suggests that reliable reconstructions are in the center of the area, along the axis SW-NE (Fig. A4). Nonetheless, the RDE and N parameters could punish our results of the inversion due to relative weights of coverage. The quality of the spatial inversion of the chequerboard may be verified by simple inspection, comparing original and reconstructed images.

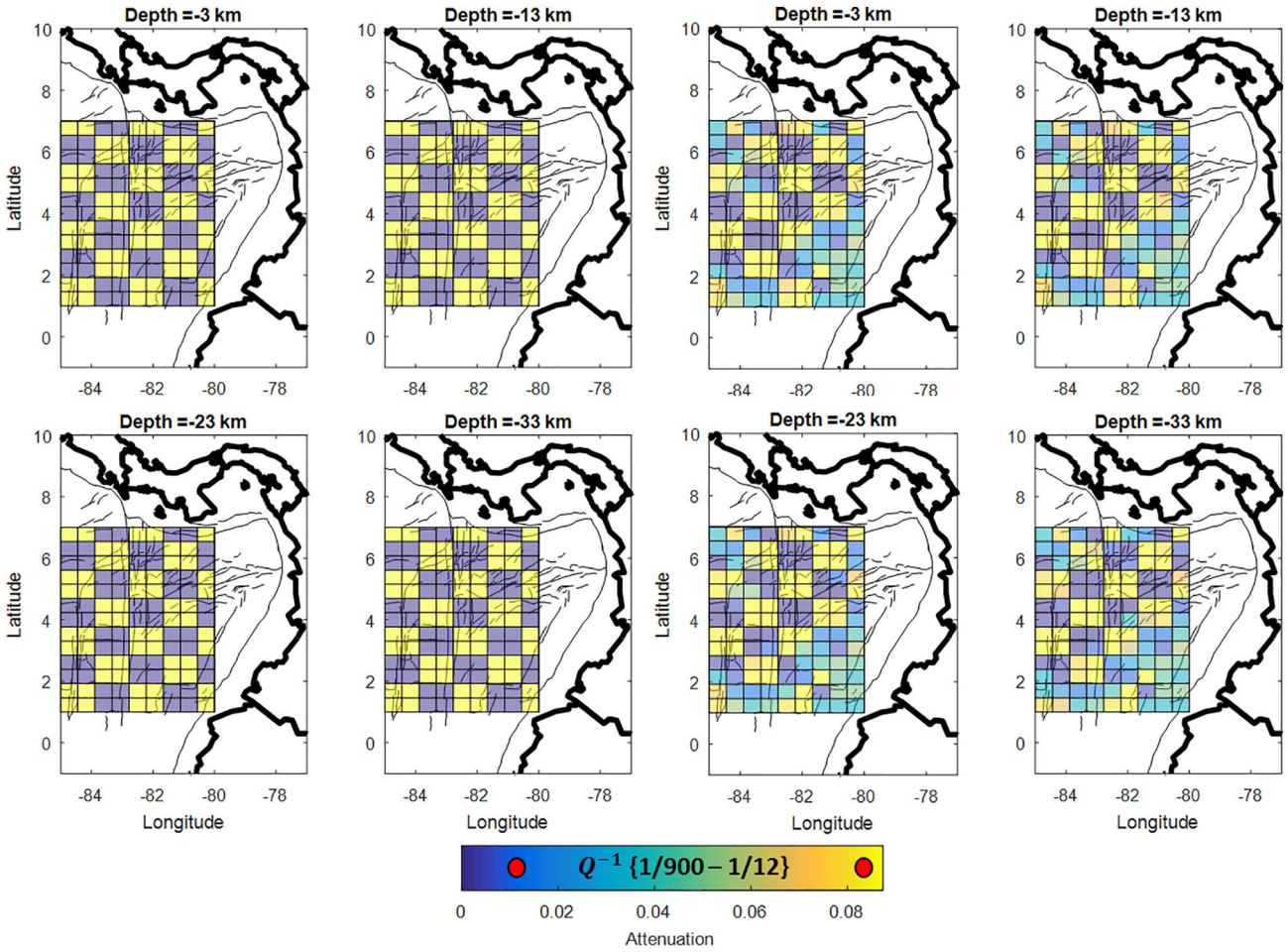

Fig. A1. Chessboard test in four layers (3, 13, 23 and 33 km in depth from the seabed) for evaluating the spatial inversion of Q_c^{-1} values under the simple back-scattering hypothesis. Inversion follows the same approach presented by Vargas and Mann (2013). Two contrasting values of attenuation (1/900 and 1/12, suggested by red points) were used for the forward problem. Inversion, based on the distribution of 529 Q_c^{-1} values (6 Hz), reconstructs almost 70% of the study area and quality slightly becomes lesser in deeper layers. Estimation was performed on a grid of 10 × 14 × 8 nodes, and each node represents the corner of a cell. (For interpretation of the references to colour in this figure legend, the reader is referred to the web version of this article.)

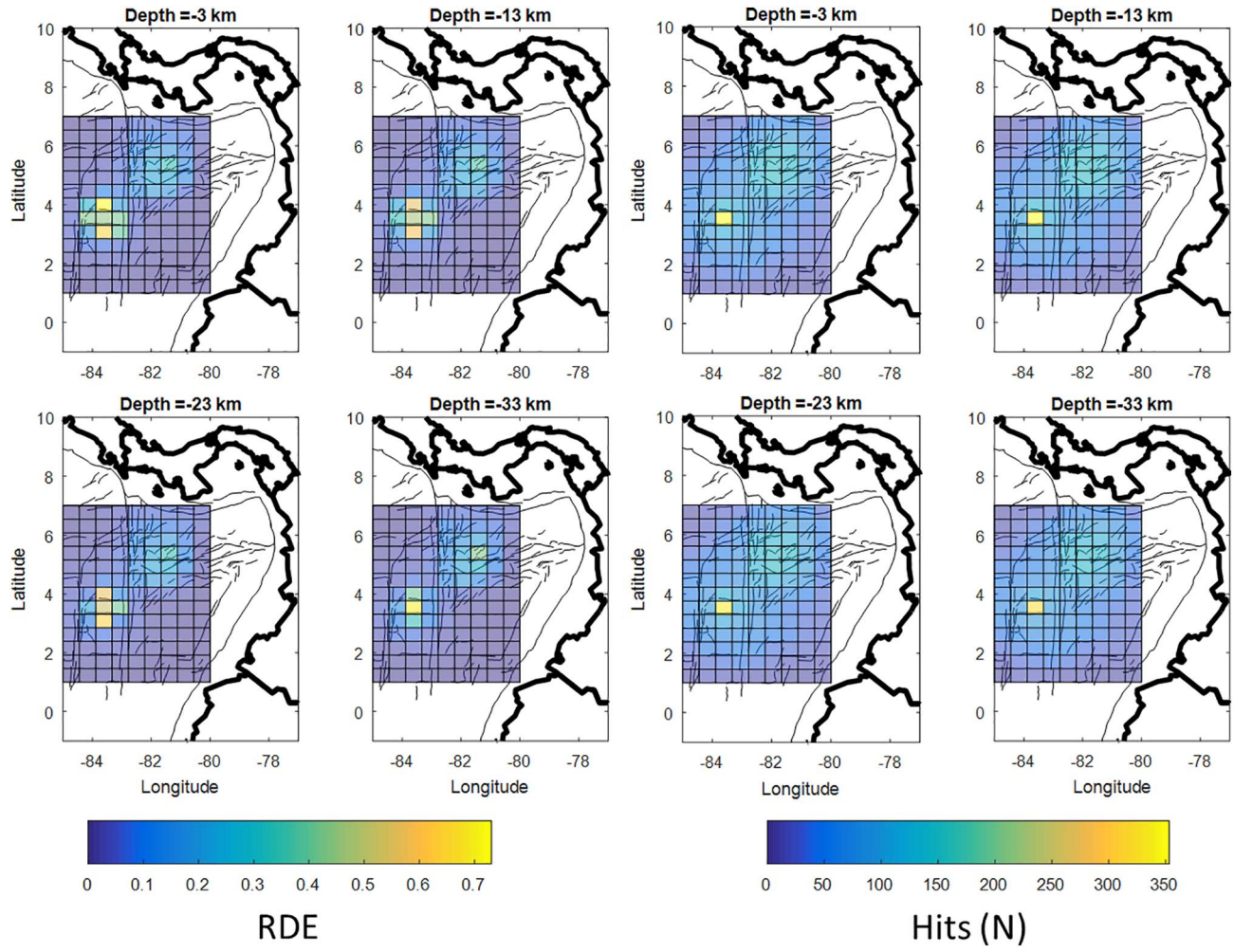

Fig. A2. Maps in-depth presenting the Resolution Diagonal Elements (RDE) derived of the spatial inversion under the simple backscattering model (on the left), and the number of times that ellipsoidal shells crossed each cell (on the right). Thought two yellow spots suggest oversampled areas, dataset confirms broad coverage that supporting the quality of the inversion. (For interpretation of the references to colour in this figure legend, the reader is referred to the web version of this article.)

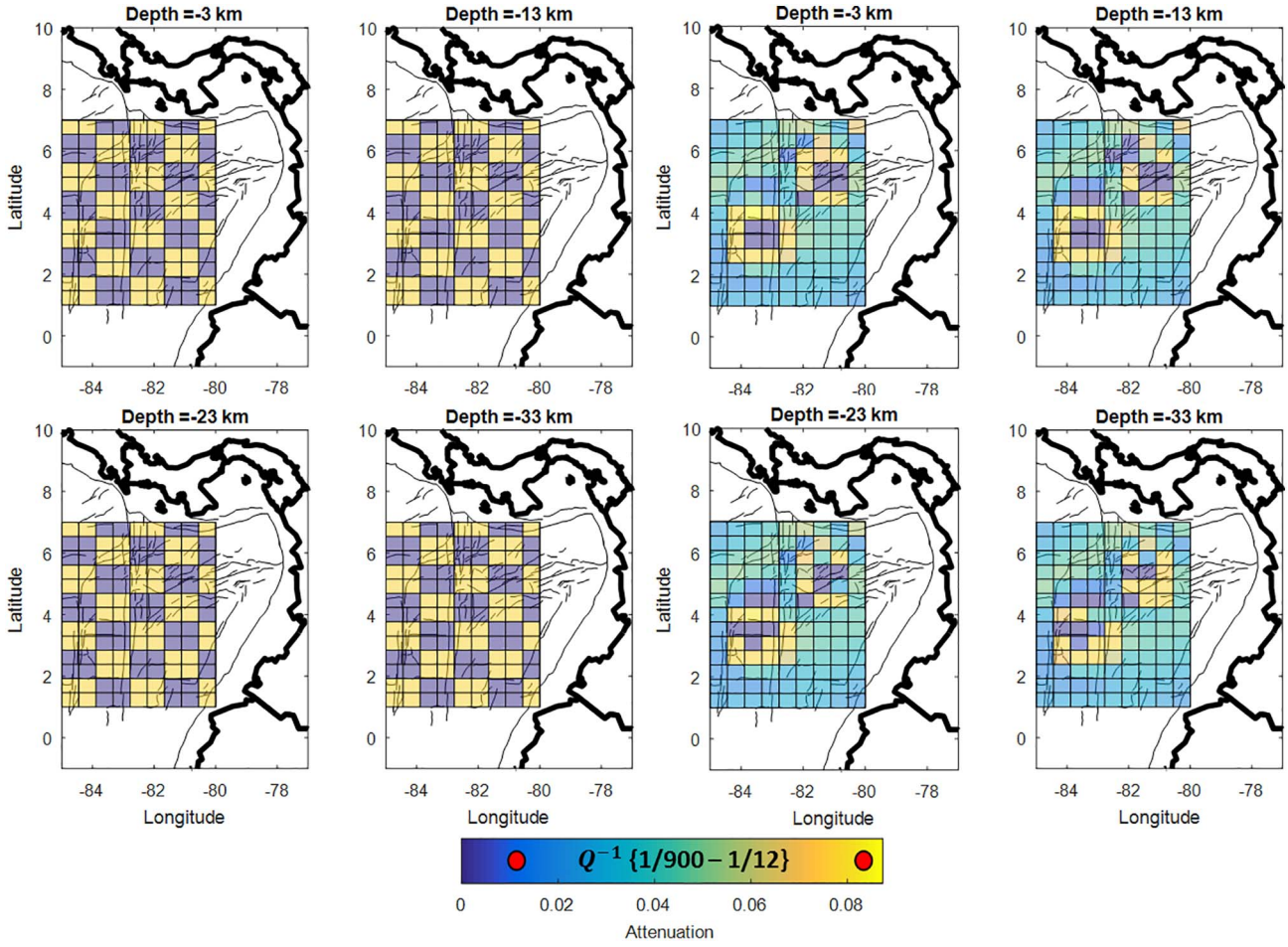

Fig. A3. Chessboard test for evaluating the spatial inversion of Q_c^{-1} values under the multiple scattering hypothesis. Inversion follows the same approach presented by Prudencio et al. (2013). Two contrasting values of attenuation (1/900 and 1/12, suggested by red points) were used for the forward problem. Inversion, based on the distribution of 529 Q_c^{-1} values (6 Hz), reconstructs < 35% of the study area and quality becomes poor in deeper layers. (For interpretation of the references to colour in this figure legend, the reader is referred to the web version of this article.)

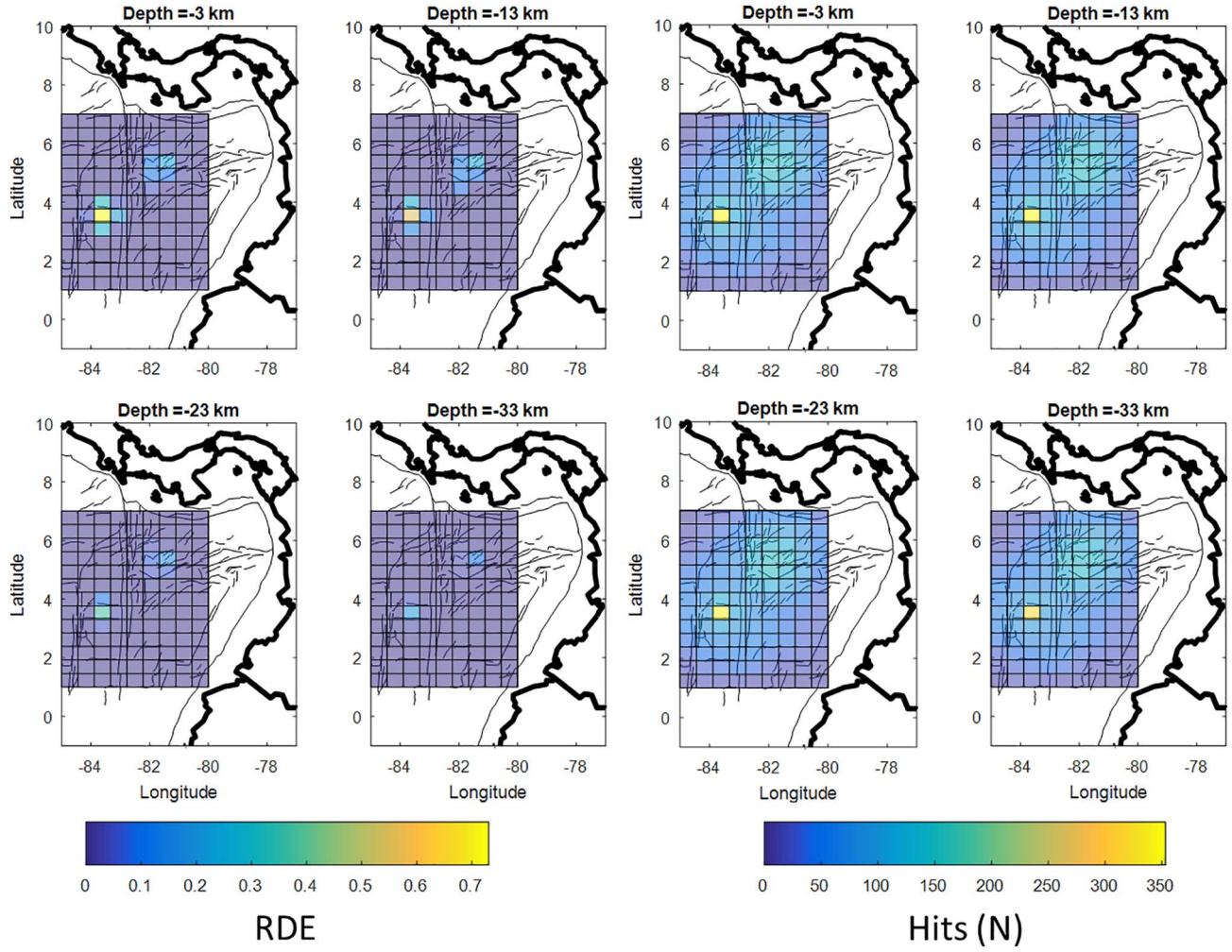

Fig. A4. Maps in-depth presenting the Resolution Diagonal Elements (RDE) derived of the spatial inversion under the multiple scattering model (on the left), and the number of times that ellipsoidal shells crossed each cell (on the right). Yellow spots persist and suggest oversampled areas. Spatial inversion and these maps indicate that the dataset is not properly distributed for covering the entire area. (For interpretation of the references to colour in this figure legend, the reader is referred to the web version of this article.)

As we expect, the multiple scattering hypothesis concentrates the attenuation along the path that connects the foci, and suppresses weak signals away of these specific areas. Vargas et al. (2004), (Fig. 5) used Monte Carlo simulations to illustrate that for lower orders of scattering broader areas are sampled and vice-versa. Hence we infer that in the extreme case, there is a concentration of the multiple scattering along the corridor that connects the foci (or a tube in 3D) that represents the spatial distribution of attenuation. This idea was developed in 2D by Calvet et al. (2013) by using simple averages of Q^{-1} values on cells distributed along the path of foci. We extend this approach to 3D. To test this approach, we used elongated pip-like ellipsoids between the foci and tried to reconstruct the original imaging with our available dataset. Fig. A5 shows several areas with contrasting attenuation values that match the original synthetic attenuation distribution. However, the general reconstruction is poor, but we think that it is limited by the geographical distribution of our dataset.

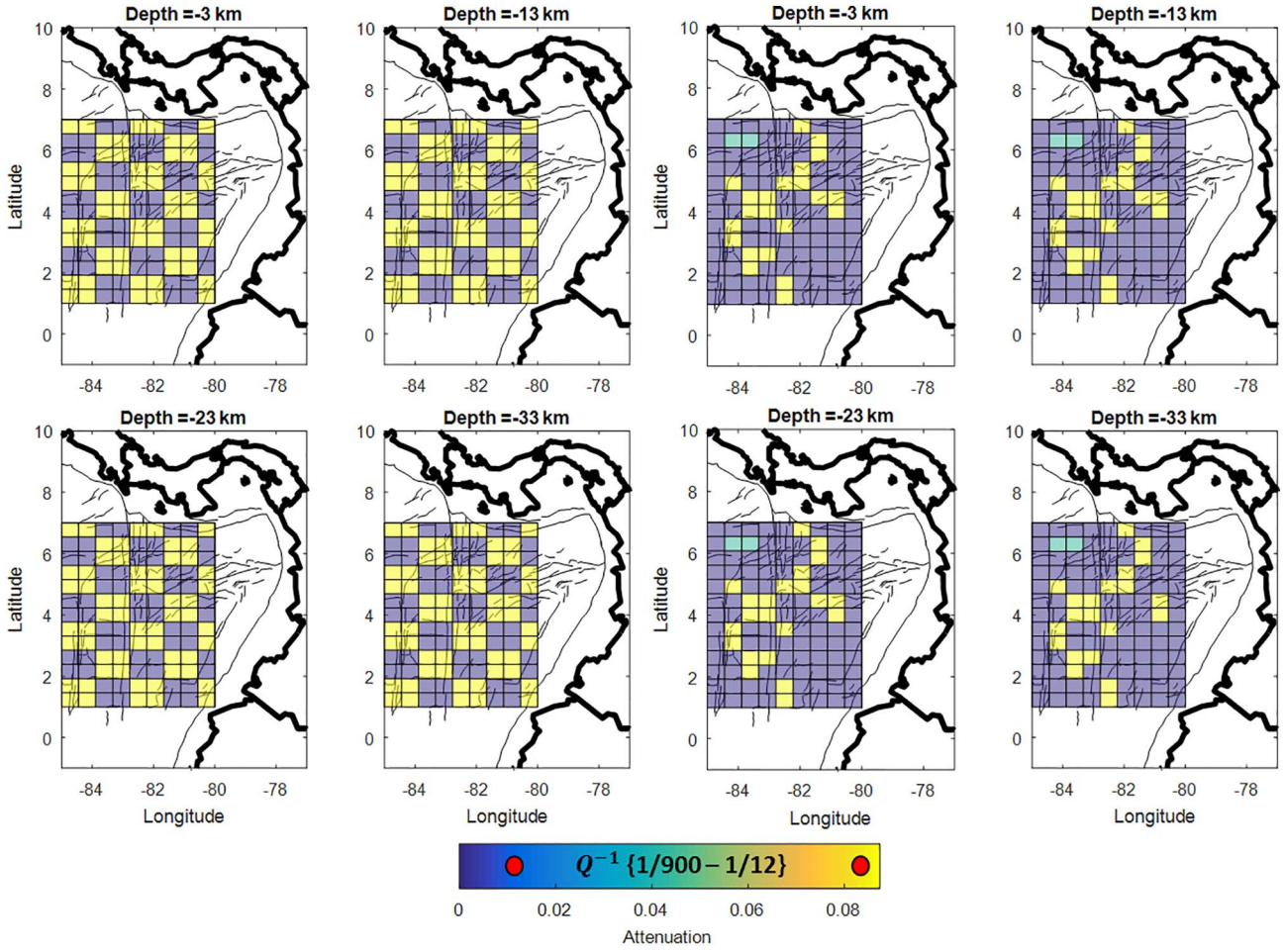

Fig. A5. Chessboard test for evaluating the spatial inversion of Q_c^{-1} values under the multiple scattering hypothesis and using the pipe-like concept derived from Calvet et al. (2013). Results of the inversion are comparable with the Prudencio et al. (2013) approach.

Differences between images estimated by the Vargas and Mann (2013) approach and the pipe-like reconstruction are not significant. Nevertheless, in both cases weak attenuation signals are punished or cancelled by the inversion, which is not be enough to explain the spatial distribution of the attenuation in our region. In fact, using the simple Gaussian type weighting function in the first approach, we recognize the existence of attenuation signals, but they are underestimated and we lose the chance to use them to identify attenuation properties away from the areas that connect the foci.

Based on the above analysis, as well as the limited dataset available and distribution of foci in this work, it was not possible to robustly estimate the spatial distribution for Q_S^{-1}, Q_{sc}^{-1} and Q_{in}^{-1}. However, given the comparable estimates of Q_c^{-1} and Q_{in}^{-1} we proceed in estimating only images of Q_c^{-1} based on the simple backscattering hypothesis for inferring intrinsic attenuation processes.

Finally, we evaluate the role of the highest attenuation values in the spatial inversion. As we noted that high Q_c^{-1} values are related to lower lapse time windows (see Fig. 5), these values may unduly contribute to anomalies near to the foci. Fig. A6 shows a comparison of two inversions using the real dataset, one of them including all the 529 observations and the other one excluding highest attenuation values (e.g. $Q_c^{-1} < 1/20$, which accounts for 7 values, just over 1% of the total dataset). Exclusion of these points makes a significant difference to the apparent attenuation. The maximum values are reduced by about a factor of 2, and other structure becomes apparent, e.g. the W-E low attenuation band in the center of the study area. Without good reason to exclude these highest attenuation values, we have chosen to use the entire dataset for our analysis and interpretations presented here. However, we think that in cases of specific interpretation, it may be possible to exclude some attenuation limits to highlight some otherwise hidden structures. The dataset used, as well as results of the inversion in MATLAB® format are provided to readers as supplemental material, so the reader can evaluate the significance of this choice.

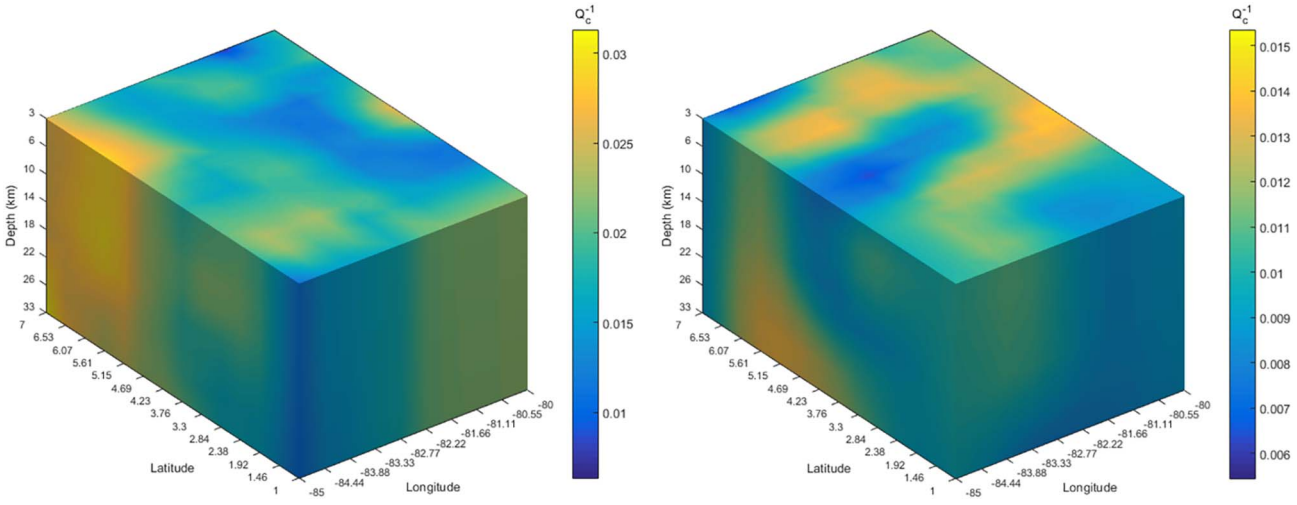

Fig. A6. Comparison between inversions using full dataset (left side) and excluding high attenuation values (right side, where in this example $Q_c^{-1} < 1/20$, which apart 7 values of the full dataset). If there is not considering a proper attenuation scale, results could pass as artifacts (see e.g. the contrasting W-E low attenuation band in the center of the study area, which is consistent if we compare values of anomalies).

Table Appendix A. Technical characteristics of the seismological stations used in this work. PSN: Panama Seismological Network; CSN: Colombia Seismological Network; ESN: Ecuador Seismological Network; USGS: US Geological Survey.

Name	Latitude (°)	Longitude (°)	High (masl)	Network	Location description	Instruments	Sampling (s)	Fo (Hz)
SR01	5.209	−81.541	−3881	OSCAR	Passive experiment	Sercel L-28 4.5 Hz Geophone/LC-2000 OBS	250	4.5
SR02	5.180	−81.205	−3412	OSCAR	Passive experiment	Sercel L-28 4.5 Hz Geophone/LC-2000 OBS	250	4.5
SR03	4.498	−81.204	−3824	OSCAR	Passive experiment	Sercel L-28 4.5 Hz Geophone/LC-2000 OBS	250	4.5
SR04	4.300	−82.001	−3993	OSCAR	Passive experiment	Sercel L-28 4.5 Hz Geophone/LC-2000 OBS	250	4.5
0057	3.222	−83.492	−3500	OSCAR	Active experiment	Sercel L-28 4.5 Hz Geophone/LC-2000 OBS	250	4.5
0063	3.032	83.496	−3500	OSCAR	Active experiment	Sercel L-28 4.5 Hz Geophone/LC-2000 OBS	250	4.5
0040	4.003	83.497	−3500	OSCAR	Active experiment	Sercel L-28 4.5 Hz Geophone/LC-2000 OBS	250	4.5
0044	3.148	83.496	−3500	OSCAR	Active experiment	Sercel L-28 4.5 Hz Geophone/LC-2000 OBS	250	4.5
AZU	7.473	−80.163	14	PSN	Azuero, Panamá	Streckeisen STS-2/Quanterra 330HR Lin	40	0.05
BCIP	9.167	−79.837	61	USGS	Barro Colorado Island, Panama	Streckeisen STS-2/Quanterra 330HR Lin	40	0.05
PNME	8.292	−80.196	79	PSN	Penonome, Panama	Streckeisen STS-2/Quanterra 330HR Lin	40	0.05
UPA	8.589	−79.320	41	PSN	Universidad de Panama, Panama	Streckeisen STS-2/Quanterra 330HR Lin	40	0.05
UPD2	8.329	−78.009	86	PSN	Meteti, Panama	Streckeisen STS-2/Quanterra 330HR Lin	40	0.05
MAL	4.008	−77.201	75	CSN	Malaga, Colombia	Streckeisen STS-2/Quanterra 330HR Lin	30	0.05
PTA	7.088	−77.485	78	CSN	Punta Ardita, Colombia	Streckeisen STS-2/Quanterra 330HR Lin	40	0.05
SOL	6.136	−77.245	38	CSN	Bahia Solano, Colombia	Streckeisen STS-2/Quanterra 330HR Lin	40	0.05
TUM	1.836	−78.726	50	CSN	Tumaco, Colombia	Streckeisen STS-2/Quanterra 330HR Lin	30	0.1
MAP	4.002	−81.610	137	CSN	Malpelo Island, Colombia	Streckeisen STS-2/Quanterra 330HR Lin	40	0.1
PIZC	4.965	−77.360	38	CSN	Pizarro, Colombia	Streckeisen STS-2/Quanterra 330HR Lin	20	0.1
DRK0	9.263	−83.245	1468	ESN	Cerro Durika, Talamanca, Puntarenas, Ecuador	CMG-6T/DM-24 Mk3 Fixed Gain	50	0.1
POTG	9.053	−83.119	674	ESN	Potrero Grande, Puntarenas, Ecuador	Episensor/Quanterra 330HR Lin	20	0.1
PIRO	8.411	−83.320	235	ESN	Piro, Osa Puntarenas, Ecuador	Trillium_compact_OBS_SIO/Taurus Infinite 40 V	30	0.4
RMG0	9.590	−82.607	17	ESN	Gandoca, Ecuador	CMG-3B/DM-24 Mk3 Fixed Gain,	50	0.4
QPSB	9.392	−84.124	52	ESN	Quepos, Puntarenas, Ecuador	Trillium_compact_OBS_SIO/Taurus Infinite 40 V	30	0.4
PAYG	−0.405	−90.172	270	ESN	Puerto Ayora, Galapagos Islands, Ecuador	Streckeisen STS-2.5/Kinemetrics FBA ES-T/ EpiSensor accelerometer	50	0.02

B. CPD values and errors associated

In general terms, within the central area of the Panama Basin errors are comparable with the estimated CPD values, in contrast with values in continental margins (Fig. B1) where the errors are smaller. The trends are consistent with what it is expected about the distribution of this isotherm

in basins near to converging regions, with shallower CPD under the younger oceanic crust and where is magmatic or hydrothermal activity, and deeper toward continental areas. The smoothed character of the CPD isotherm reported in this work is due to the low resolution of the dataset used (Maus et al., 2007; Dyment et al., 2015), and the stacking of analyzed 2D spatial windows.

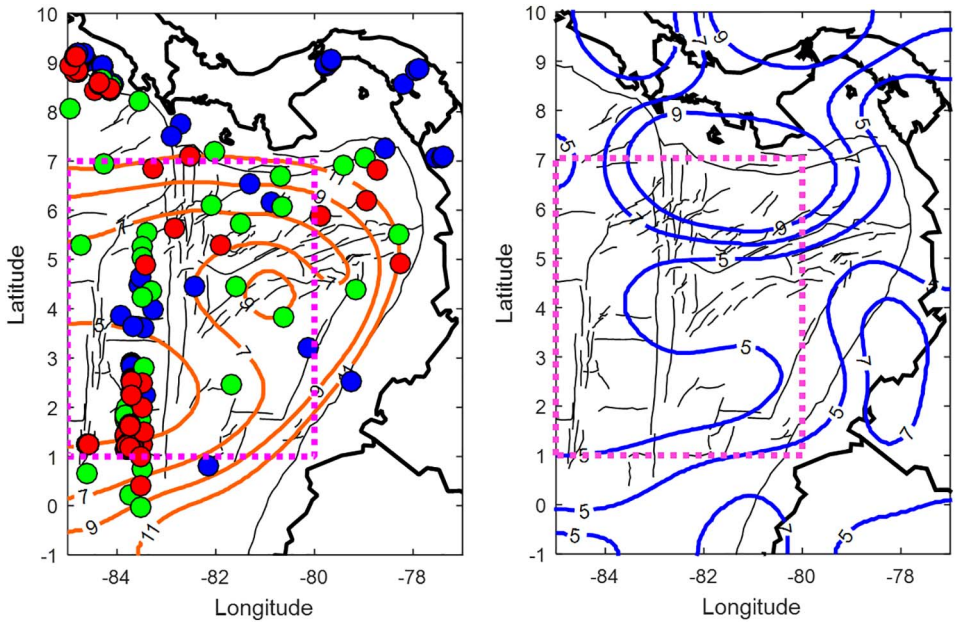

Fig. B1. Results of the Curie Depth Point estimations (CPD - in km is presented in light brown with numbers) using the dataset compiled in the WDMAM (Maus et al., 2007; Dyment et al., 2015). CPD map (left) is overlapped with heat flow observations. Coloured dots correspond to heat flow measurements presented in three ranges. Low (blue): HF $< 100\,mW/m^2$; intermedium (green): HF $\geq 100\,mW/m^2$ and HF $< 200\,mW/m^2$; and high (red): HF $\geq 200\,mW/m^2$. Purple and dashed polygons represent the area where was estimated the attenuation tomography. Errors associated with the CPD calculations are presented in heavy blue lines with numbers (right). (For interpretation of the references to colour in this figure legend, the reader is referred to the web version of this article.)

The CPD isotherm becomes shallower at the SW, in areas where is reported a contrasting thermal activity (Kolandaivelu et al., 2017). It is also noteworthy that under the MR this isotherm is deeper, suggesting a locally lower heat flow and/or thicker crust.

References

Aki, K., 1980. Attenuation of shear-waves in the lithosphere for frequencies from 0.05 to 25 Hz. Phys. Earth Planet. Inter. 21 (1), 50–60. http://dx.doi.org/10.1016/0031-9201(80)90019-9.

Aki, K., Chouet, B., 1975. Origin of the coda waves: source attenuation and scattering effects. J. Geophys. Res. 80, 3322–3342.

Akinci, A., Taktak, A., Ergintav, S., 1994. Attenuation of coda waves in western anatolia. Phys. Earth Planet. Inter. 87 (12), 155–165. http://dx.doi.org/10.1016/0031-9201(94)90028-0.

Artemieva, I.M., Billien, M., Leveque, J.J., Mooney, W.D., 2004. Shear wave velocity, seismic attenuation, and thermal structure of the continental upper mantle. Geophys. J. Int. 157, 607–628. http://dx.doi.org/10.1111/j.1365-246X.2004.02195.x.

Blakely, R.J., 1996. Potential Theory in Gravity andMagnetic Applications. Cambridge University Press.

Calvet, M., Sylvander, M., Margerin, L., Villasenor, A., 2013. Spatial variations of seismic attenuation and heterogeneity in the Pyrenees: coda Q and peak delay time analysis. Tectonophysics 608, 428–439.

Davis, E.E., Becker, K., He, J., 2004. Costa Rica Rift revisited: constraints on shallow and deep hydrothermal circulation in young oceanic crust. Earth Planet. Sci. Lett. 222, 863–879.

Del Pezzo, E., 2008. Earth heterogeneity and scattering effects of seismic waves: seismic wave scattering in volcanoes. Adv. Geophys. 50, 353–371.

Del Pezzo, E., Ibañez, J., Prudencio, J., Bianco, F., De Siena, L., 2016. Absorption and scattering 2-D volcano images from numerically calculated space-weighting functions. Geophys. J. Int. 206 (2), 742–756. http://dx.doi.org/10.1093/gji/ggw171.

Dyment, J., Lesur, V., Hamoudi, M., Choi, Y., Thebault, E., Catalan, M., 2015. World Digital Magnetic Anomaly Map. map available at. http://www.wdmam.org, version 2.0.

Eberhart-Phillips, D., Michael, A.J., 1993. Three-dimensional velocity structure, seismicity, and fault structure in the Parkfield region, central California. J. Geophys. Res. 98 (B9), 15,737–15,758.

Ekström, G., Nettles, M., Dziewonski, A.M., 2012. The global CMT project 2004–2010: centroid-moment tensors for 13,017 earthquakes. Phys. Earth Planet. Inter. 200–201, 1–9. http://dx.doi.org/10.1016/j.pepi.2012.04.002.

Fehler, M., Sato, H., 2003. Coda. Pure Appl. Geophys. 160 (2003), 541–554.

Hardy, N.C., 1991. Tectonic evolution of the easternmost Panama Basin: some new data and inferences. J. S. Am. Earth Sci. 4 (3), 261–269.

Hasterok, D., Chapman, D.S., Davis, E.E., 2011. Oceanic heat flow: implications for global heat loss. Earth Planet. Sci. Lett. 311, 386–395.

Hobbs, R.W., Peirce, C., 2015. RRS James Cook JC114 Cruise Report, 2015.

Hoshiba, M., 1991. Simulation of multiple scattered coda wave excitation based on the energy conservation law. Phys. Earth Planet. Inter. 67, 123–136.

Hurt, C.P., Moskowitz, B.M., Banerjee, S.K., 1995. Magnetic properties of rocks and minerals. Rock physics and phase relations. In: A Handbook of Physical Constants 3. AGU Reference Shelf, pp. 189–204.

Jackson, I., Paterson, M.S., Fitz Gerald, J.D., 1992. Seismic wave dispersion and attenuation in Åheim dunite: an experimental study. Geophys. J. Int. 108 (1992), 517–534.

Jin, A., Aki, K., 1988. Spatial and temporal correlation between coda Q and seismicity in China. Bull. Seismol. Soc. Am. 78, 741–769.

Karato, S.-I., 1993. Importance of anelasticity in the interpretation of seismic tomography. Geophys. Res. Lett. 20, 1623–1626.

Kolandaivelu, K.P., Harris, R.N., Lowella, R.P., Alhamad, A., Gregoryc, E.P.M., Hobbs, R.W., 2017. Analysis of a conductive heat flow profile in the Ecuador Fracture Zone. Earth Planet. Sci. Lett. 467, 120–127.

Lin, G., Shearer, P.M., Amelung, F., Okubo, P.G., 2015. Seismic tomography of compressional wave attenuation structure for Kīlauea Volcano, Hawai'i. J. Geophys. Res. Solid Earth 120, 2510–2524. http://dx.doi.org/10.1002/2014JB011594.

Lonsdale, P., 2005. Creation of the Cocos and Nazca plates by fission of the Farallon plate. Tectonophysics 404, 237–264.

Malin, P.E., 1978. A First Order Scattering Solution for Modeling Lunar and Terrestrial Seismic Codas (PhD thesis). Princeton University.

Maule, C.F., Purucker, M.E., Olsen, N., Mosegaard, K., 2005. Heat flux anomalies in Antarctica revealed by satellite magnetic data. Science 309, 464–467.

Maus, S., Sazonova, T., Hemant, K., Fairhead, J.D., Ravat, D., 2007. National geophysical data center candidate for the world digital magnetic anomaly map. Geochem. Geophys. Geosyst. 8, Q06017. http://dx.doi.org/10.1029/2007GC001643.

Mukhopadhyay, S., Sharma, J., Massey, R., Kayal, J.R., 2008. Lapse time dependence of coda Q in the source region of the 1999 Chamoli earthquake. Bull. Seismol. Soc. Am. 98 (4), 2080–2086. http://dx.doi.org/10.1785/0120070258.

O'Brien, G., Bean, C.J., 2009. Volcano topography, structure and intrinsic attenuation: their relative influences on a simulated 3D visco-elastic wavefield. J. Volcanol. Geotherm. Res. 183, 122–136.

Okubo, Y., Matsunaga, T., 1994. Curie point depth in northeast Japan and its correlation

with regional thermal structure and seismicity. J. Geophys. Res. Solid Earth 99 (B11), 22363–22371.
Okubo, Y., Graf, R.J., Hansen, R.O., Ogawa, K., Tsu, H., 1985. Curie point depths of the island of Kyushu and surrounding areas, Japan. Geophysics 50 (3), 481–494.
Ottemöller, L., Voss, P., Havskov, J., 2016. Seisan Earthquake Analysis Software for Windows, Solaris, Linux and MacosX. http://seisan.info, Version 10.5.
Prudencio, J., Del Pezzo, E., García-Yeguas, A., Ibáñez, J.M., 2013. Spatial distribution of intrinsic and scattering seismic attenuation in active volcanic islands, I: model and the case of Tenerife Island. Geophys. J. Int. 195 (3), 1942–1956. http://dx.doi.org/10.1093/gji/ggt361.
Pujades, L.G., Canas, J.A., Egozcue, J.J., Puigvi, M.A., Gallart, J., Lana, X., Pous, J., Casas, A., 1990. Coda-Q distribution in the Iberian Peninsula. Geophys. J. Int. 100, 285–301.
Pujol, J., 2007. The solution of nonlinear inverse problems and the Levenberg-Marquardt method. Geophysics. SEG. 72 (4), W1–W16. http://dx.doi.org/10.1190/1.2732552.
Pulli, J.J., 1984. Attenuation of coda waves in New England. Bull. Seismol. Soc. Am. 74, 1149–1166.
Rautian, T.G., Khalturin, V.I., 1978. The use of the coda for determination of the earthquake source spectrum. Bull. Seismol. Soc. Am. 68 (4), 923–948.
Ravat, D., 2004. Constructing full spectrum potential-field anomalies for enhanced geodynamical analysis through integration of surveys from different platforms. In: AGU Fall Meeting Abstracts December.
Roecker, S.W., Tucker, B., King, J., Hatzfeld, D., 1982. Estimates of q in central asia as a function of frequency and depth using the coda of locally recorded earthquakes. Bull. Seismol. Soc. Am. 72 (1), 129–149.
Ross, H.E., Blakely, R.J., Zoback, M.D., 2004. Testing the utilization of aeromagnetic data for the determination of Curie-isotherm depth. In: AGU Fall Meeting Abstracts. Vol. 1. pp. 1287 (December)w.
Ruiz, R., Introcaso, A., 2004. Curie point depths beneath Precordillera Cuyana and Sierras Pampeanas obtained from spectral analysis of magnetic anomalies. Gondwana Res. 7 (4), 1133–1142.
Salazar, J.M., Vargas, C.A., Leon, H., 2017. Curie point depth in the SWCaribbean using the radially averaged spectra of magnetic anomalies. Tectonophysics 694, 400–413. http://dx.doi.org/10.1016/j.tecto.2016.11.023.
Sato, H., Fehler, M.C., 2009. Seismic Wave Propagation and Scattering in the Heterogenous Earth. Springer Ed (308pp).
Sato, H., Sacks, I.S., Murase, T., Muncill, G., Fukuyama, H., 1989. Qp melting temperature relation in peridotite at high pressure and temperature: attenuation mechanism and implications for the mechanical properties of the upper mantle. J. Geophys. Res. 94, 10647–10661.
Sato, H., Fehler, M.C., Maeda, T., 2012. Seismic Wave Propagation and Scattering in the Heterogeneous Earth, Second Edition. Springer (494 pp). https://doi.org/10.1007/978-3-642-23029-5.
Singh, S., Herrmann, R.B., 1983. Regionalization of crustal coda Q in the continental United States. J. Geophys. Res. 88, 527–538.
Singh, C., Mukhopadhyay, S., Singh, S., Chakraborty, P., Kayal, J., 2014. Study of lapse time dependence Coda Q in the Andaman Islands using the aftershocks of the 2002 earthquake (Mw 6.5). Nat. Hazards 1–15. http://dx.doi.org/10.1007/s11069-014-1337-7.
Spector, A., Grant, F.S., 1970. Statistical models for interpreting aeromagnetic data. Geophysics 35 (2), 293–302.
Sutherland, R., et al., 2017. Extreme hydrothermal conditions at an active plate-bounding fault. Nat. Lett. http://dx.doi.org/10.1038/nature22355.
Tanaka, A., Okubo, Y., Matsubayashi, O., 1999. Curie point depth based on spectrum analysis of the magnetic anomaly data in East and Southeast Asia. Tectonophysics 306, 461–470.
Thurber, C., Eberhart-Phillips, D., 1999. Local earthquake tomography with flexible gridding. Comput. Geosci. 25, 809–818.
Tselentis, G.-A., 1998. Intrinsic and scattering seismic attenuation in W. Greece. Pure Appl. Geophys. 153, 703–712.
Tsujura, M., 1966. Frequency analysis of seismic waves. Bull. Earthquake Res. Inst. Tokyo Univ. 44, 873–891.
Turcotte, D., Schubert, G., 2014. Geodynamics, Third Ed. Cambridge University Press (639 pp).
Vargas, C.A., Mann, P., 2013. Tearing and breaking off of subducted slabs as the result of collision of the Panama arc-indenter with northwestern South America. Bull. Seismol. Soc. Am. 103 (3), 2025–2046. http://dx.doi.org/10.1785/0120120328.
Vargas, C.A., Ugalde, A., Pujades, L.G., Canas, J.A., 2004. Spatial variation of coda wave attenuation in northwestern Colombia. Geophys. J. Int. 158, 609–624. http://dx.doi.org/10.1111/j.1365-246X.2004.02307.x.
Vargas, C.A., Idarraga-Garcia, J., Salazar, J.M., 2015. Curie point depth in northwestern South America and the southwestern Caribean Sea. In: Bartolini, C., Mann, P. (Eds.), Petroleum Geology and Potential of the Colombian Caribbean Margin, pp. 179–200 AAPG Memoir 108, Chapt. 7. (ISBN13: 978-0-89181-388-0).
Wang, Z., Zhao, D., Liu, X., Chen, C., Li, X., 2017. P and S-wave attenuation tomography of the Japan subduction zone. Geochem. Geophys. Geosyst. 18. http://dx.doi.org/10.1002/2017GC006800.
Wennerberg, L., 1993. Multiple-scattering interpretation of coda-Q measurements. Bull. Seismol. Soc. Am. 83, 279–290.
Yang, K., Xing, J., Gong, W., Li, C., Wu, X., 2017. Curie point depth from spectral analysis of magnetic data in the Southeast Tibet. Earth Sci. 6 (5), 88–96. http://dx.doi.org/10.11648/j.earth.20170605.15.
Zeng, Y., 1991. Compact solutions for multiple scattered Wa6e energy in time domain. Bull. Seismol. Soc. Am. 81, 1022–1029.